The Gibbs free energy landscape based on liver metabolome revealed thermodynamic robustness against fasting and obesity

AUTHORS

Takumi Abekawa[1], Satoshi Ohno[1,2,3,*], Akiyoshi Hirayama[4], Tomoyoshi Soga[4,5], Shinya Kuroda[1,2,6,*]

AFFILIATIONS

[1]Department of Biological Sciences, Graduate School of Science, The University of Tokyo, 7-3-1 Hongo, Bunkyo-ku, Tokyo 113-0033, Japan.

[2]Molecular Genetics Research Laboratory, Graduate School of Science, The University of Tokyo, 7-3-1 Hongo, Bunkyo-ku, Tokyo, Japan.

[3]Life Science Center for Survival Dynamics, Tsukuba Advanced Research Alliance (TARA), University of Tsukuba, 1-1-1 Tennodai, Tsukuba, Ibaraki 305-8577, Japan.

[4]Institute for Advanced Biosciences, Keio University, 246-2 Mizukami, Kakuganji, Tsuruoka, Yamagata 997-0052, Japan

[5]Human Biology-Microbiome-Quantum Research Center (WPI-Bio2Q), Keio University, Tsuruoka, Yamagata 997-0052, Japan

[6]Lead contact

[*]Correspondence to: s-ohno@tara.tsukuba.ac.jp (S.O.)

[*]Correspondence to: skuroda@bs.s.u-tokyo.ac.jp (S.K.)

SUMMARY

Mammalian liver metabolism undergoes a substantial shift during fasting. Thermodynamic principles impose fundamental constraints on metabolism, and the Gibbs free energy change of reaction ($\Delta_r G'$) indicates the reaction's direction and distance from equilibrium. However, $\Delta_r G'$ landscapes in intact mammalian organs remain largely uncharacterized. Here, we mapped $\Delta_r G'$ profile of glucose metabolism in mouse liver during fasting, using experimentally measured absolute metabolite concentrations and a newly developed computational method, GLEAM. We found that despite large metabolite fluctuations during fasting, the corresponding $\Delta_r G'$s remained robust, even for reactions reversing the direction between glycolysis and gluconeogenesis. A remarkable thermodynamic robustness is found in maintaining potential candidates of rate-limiting steps during fasting. This robustness is achieved by expending substantial costs for enzyme expressions, contributing to efficient switching from glycolysis to gluconeogenesis. Furthermore, obese mouse liver also showed thermodynamic robustness despite obesity-induced metabolic disruption. Our framework provided a novel thermodynamic perspective on intact organ metabolism, demonstrating that the liver robustly maintains thermodynamic characteristics favorable for metabolic control by buffering metabolite concentration differences.

41 **GLOSSARY**

Metabolite abbreviations	Metabolite names
G6P	Glucose 6-phosphate
F6P	Fructose 6-phosphate
F1,6BP	Fructose 1,6-bisphosphate
ADP	ADP
ATP	ATP
DHAP	Glycerone phosphate
GAP	Glyceraldehyde 3-phosphate
NAD	NAD^+
NADH	NADH
Pi	Orthophosphate
3PG	3-Phospho-D-glycerate
2PG	2-Phospho-D-glycerate
PEP	Phosphoenolpyruvate
H2O	H2O
G1P	Glucose 1-phosphate
G3P	sn-Glycerol 3-phosphate
Pyr	Pyruvate
CoA	Coenzyme A
CO2	CO2
AcCoA	Acetyl-CoA

OAA	Oxaloacetate
Cit	Citrate
AKG	alpha-Ketoglutaric acid
SucCoA	Sucinyl-CoA
Suc	Succinate
GDP	GDP
GTP	GTP
Fum	Fumarate
FAD	FAD
FADH2	FADH2
Mal	Malate
Glu	Glutamate
NH3	Ammonia
Ala	L-Alanine
Lac	Lactate
HCO3	HCO_3^-
NADP	$NADP^+$
NADPH	NADPH

Reaction abbreviations	Reaction names
GLUT	Glucose transporter
GCK	Glucokinase

HK	Hexokinase
GPI	Glucose-6-phosphate isomerase
PFK	Phosphofructokinase
ALDO	Aldolase
TPI	Triosephosphate isomerase
GAPDH:PGK	Glyceraldehyde-3-phosphate dehydrogenase and Phosphoglycerate kinase
PGAM	Phosphoglycerate mutase
ENO	Enolase
PGM	Phosphoglucomutase
FBP	Fructose-1,6-bisphosphatase
G6PC	Glucose-6-phosphatase
GPD	Glycerol-3-phosphate dehydrogenase
PKLR	Pyruvate kinase
PDH	Pyruvate dehydrogenase
CS	Citrate synthase
ACO:IDH	Aconitase and Isocitrate dehydrogenase
OGDH	2-Oxoglutarate dehydrogenase
LSC	Succinate-CoA ligase
SDH	Succinate dehydrogenase
FH	Fumarate hydratase
MDH	Malate dehydrogenase
GDH	Glutamate dehydrogenase

ALT	Alanine aminotransferase
LDH	Lactate dehydrogenase
MCT	Monocarboxylate transporter
PC	Pyruvate carboxylase
PCK	Phosphoenolpyruvate carboxykinase
ME	Malic enzyme

42

INTRODUCTION

Blood glucose homeostasis is crucial in mammals for providing stable energy sources to organs and maintaining health. During fasting, the liver plays a central role in maintaining blood glucose homeostasis by shifting its metabolism from glycolysis to gluconeogenesis [1–5]. This metabolic shift is a highly regulated process that involves the directional reversal of metabolic reactions and fluctuations in the concentrations of numerous metabolites [6–8]. Obesity induces metabolic dysregulation in the liver [7–12], leading to impaired glucose homeostasis [13–17] and the development of further diseases, including type 2 diabetes [9,18–20].

Metabolic processes are governed by the laws of thermodynamics. According to the second law of thermodynamics, in the cellular environment, metabolic reactions proceed in the direction where the Gibbs free energy change of reaction ($\Delta_r G'$) is negative, and $\Delta_r G'$ is zero when the reaction reaches equilibrium. Therefore, $\Delta_r G'$ indicates the reaction distance from equilibrium. $\Delta_r G'$ can be calculated as the difference between the Gibbs free energy of formation ($\Delta_f G'$) of the product and substrate metabolites:

$$\Delta_r G' = \sum_i S_i \Delta_f G'_i \tag{1}$$

where S_i is the stoichiometric coefficient of metabolite i in the reaction. $\Delta_f G'$ depends on the metabolite activity, practically substituted by the concentration:

$$\Delta_f G' = \Delta_f G'^{\circ} + RT \ln c \tag{2}$$

where $\Delta_f G'^{\circ}$ is the standard Gibbs free energy of formation representing $\Delta_f G'$ at 1 M of metabolite concentration, R is the gas constant, T is temperature, and c is metabolite

concentration. The prime placed in $\Delta_f G'^{\circ}$, $\Delta_f G'$, and $\Delta_r G'$ denotes that those values incorporate the effect of a particular pH, pMg, and ionic strength on metabolite activity. Although calculation of $\Delta_r G'$ requires absolute metabolite concentrations, mass spectrometry-based metabolomics analyses often suffer from ion suppression, a phenomenon where co-eluting compounds compromise quantitative accuracy by reducing analyte ionization efficiency [21]. Nevertheless, previous studies have successfully achieved absolute quantification of intracellular metabolites, primarily by employing isotope-labeled internal standards [22,23]. These techniques have enabled the investigation of absolute metabolite concentrations and subsequent thermodynamic analyses, such as $\Delta_r G'$ landscapes, in microorganisms and cultured cells. [24–27]. Despite these advancements, thermodynamic profiles have rarely been investigated at *in vivo* mammalian organ levels. Furthermore, all prior thermodynamic studies have focused on glycolysis-dominant conditions where glucose is the primary nutrient, leaving a large gap in our understanding of metabolism during fasting, a condition dominated by gluconeogenesis.

Mathematical metabolic modeling is an essential framework for a quantitative system-level understanding of metabolism. The thermodynamic principle regarding reaction direction has been widely applied as a constraint to increase the reliability of metabolic models [28–35]. Furthermore, the significance of $\Delta_r G'$ extends beyond physical aspects such as distance from equilibrium and reaction directionality to several physiological meanings, including pathway rate-limiting steps quantified by the flux control coefficient (FCC) [36–38], and enzyme

demands for carrying metabolic flux [39–42]. However, these thermodynamic frameworks have hardly been applied to experimental data, especially those from multicellular organisms.

In this study, we explored $\Delta_r G'$ landscape in the liver metabolism of mice at different fasting levels using time-series absolute quantitative metabolomic data measured by CE-MS, which can reduce the effect of ion suppression [43,44], without using isotopically labeled standards. Our results are the first *in vivo* identification of large-scale $\Delta_r G'$ landscapes in mammalian organisms, and also the first elucidation of $\Delta_r G'$ behavior during fasting in any cell types. Since metabolomic data contains uncertainties, we developed GLEAM (Gibbs free energy of reaction Landscape Estimation from metabolome Assisted by variance-covariance Matrix) to estimate $\Delta_r G'$ with thermodynamically consistent metabolite concentrations from experimental metabolomic data. The estimated $\Delta_r G'$ showed that the global $\Delta_r G'$ landscape in mouse liver is robust during fasting, despite large fluctuations in metabolite concentrations. We further integrated the $\Delta_r G'$ and enzyme kinetics to investigate the physiological significance of the $\Delta_r G'$ landscape in terms of rate-limiting steps and efficiency of metabolic switching. In addition to the thermodynamic robustness of mouse liver against fasting, we also demonstrated the robustness against obesity using leptin-deficient obese (*ob*/*ob*) mice [45,46]. Thus, our study provides novel insights into glucose metabolism in *in vivo* mammalian liver from a thermodynamic standpoint. These findings extend our understanding of mammalian metabolisms beyond individual metabolite concentrations.

RESULTS

$\Delta_r G'$ landscape is robust against fasting despite metabolite concentration fluctuations

In this study, we developed GLEAM to estimate $\Delta_r G'$ from time-series metabolome and $\Delta_f G'^{\circ}$. One of the challenges in estimating $\Delta_r G'$ in an entire reaction pathway is inherent uncertainties and missing values in metabolome and $\Delta_f G'^{\circ}$ data. To address this issue, GLEAM utilizes thermodynamic constraints and variances and covariances of metabolome and $\Delta_f G'^{\circ}$ data, and estimates a complete set of thermodynamically consistent metabolite concentrations and $\Delta_f G'^{\circ}$, and subsequent $\Delta_r G'$ (see Methods). Briefly, GLEAM fits metabolite concentrations and $\Delta_f G'^{\circ}$ to data from the experiment or database within a range that every reaction holds $\Delta_r G' < 0$ by the weighted least mean squares method. The weights of the residuals are determined by variances and covariances of metabolite concentrations and $\Delta_f G'^{\circ}$ data.

By applying GLEAM to time-series metabolomic data from *ad libitum* feeding to fasting in mice, and $\Delta_f G'^{\circ}$ data from eQuilibrator (Table S1), we estimated the $\Delta_r G'$ landscape (Fig. 1A, B, Table S2) in glycolysis, gluconeogenesis, and TCA cycle (Table S3) in the liver. At *ad libitum* feeding (0-hour fasting), when glycolysis is dominant, most of the irreversible reactions exhibited $\Delta_r G' < -10$ kJ/mol, which were defined as far-from-equilibrium reactions, such as $\Delta_r G' = -21.56$ kJ/mol in PFK and $\Delta_r G' = -34.34$ kJ/mol in PDH. Among the 11 irreversible reactions, only three reactions (ACO:IDH, PC, and PCK) exhibited $\Delta_r G' > -10$ kJ/mol, and PC and PCK were exceptionally close to equilibrium,

with $\Delta_r G'$ = −3.48 kJ/mol and −3.70 kJ/mol, respectively. In contrast, most of the reversible reactions exhibited $\Delta_r G'$ > −5 kJ/mol, which were defined as near-equilibrium reactions, at *ad libitum* feeding, such as $\Delta_r G'$ = −0.24 kJ/mol in GPI and $\Delta_r G'$ = −0.03 kJ/mol in SDH. Four reversible reactions (ALDO, LSC, MDH, and ME) were exceptions that exhibited $\Delta_r G'$ < −5 kJ/mol. Among those reactions, MDH was largely away from equilibrium in the opposite direction of the oxidative TCA cycle, with $\Delta_r G'$ = −18.13 kJ/mol.

The fasting-induced metabolic shift in the liver from glycolysis to gluconeogenesis may lead to changes in thermodynamic characteristics of metabolic reactions, including reversal of the sign of $\Delta_r G'$ of some reactions *i.e.,* reversal of their direction, by fluctuations in several metabolite concentrations. After 16-hour fasting when gluconeogenesis is dominant, $\Delta_r G'$ values remained similar in the liver (Fig. 1C), with variation in 24/29 reactions being less than 5 kJ/mol. As a result of this thermodynamic robustness, all irreversible reactions exhibited $\Delta_r G'$ < −10 kJ/mol after 16-hour fasting, indicating that the overall trend of irreversible reactions being far-from-equilibrium reactions was maintained across *ad libitum* feeding and after fasting. Although PC and PCK had been near-equilibrium at *ad libitum* feeding, these reactions moved away from equilibrium to exhibit $\Delta_r G'$ = −9.07 kJ/mol and −5.25 kJ/mol after fasting, respectively. As for reversible reactions, despite reversal of some directions to switch the liver's metabolism from glycolysis to gluconeogenesis, all the reversible reactions with $\Delta_r G'$ > −5 kJ/mol at *ad libitum* feeding remained $\Delta_r G'$ > −5 kJ/mol, indicating that the overall trend of reversible reactions being near-equilibrium reactions was maintained across *ad libitum* feeding and after fasting. In contrast to $\Delta_r G'$,

148 individual metabolite concentrations widely fluctuated during 16-hour fasting (Fig. 1D), with
149 log2 fold change exceeding 0.5 for over 50% of metabolites. This result suggests that the
150 thermodynamic architecture in glucose metabolism was robust against fasting while
151 metabolite concentrations were reorganized. Note that the robustness of $\Delta_r G'$ and
152 metabolite concentrations cannot be directly compared by correlation coefficients for Fig. 1C
153 and D because $\Delta_r G'$ values were not normalized while metabolite concentrations were
154 normalized, leading to much higher correlation coefficient for $\Delta_r G'$. The reason why $\Delta_r G'$
155 values were not normalized in Fig. 1C is that $\Delta_r G'$ does not represent abundance and thus
156 should be evaluated their robustness not by fold changes but by difference values.
157
158 To examine whether the thermodynamic characteristics of metabolic reactions observed in
159 mouse liver are conserved across species, we compared the estimated $\Delta_r G'$ in glycolytic
160 reactions in mouse liver with those in other biological systems. The previous study [26]
161 determined $\Delta_r G'$ in glycolysis of immortalized baby mouse kidney epithelial (iBMK) cells,
162 yeast, and *Escherichia coli*, reporting that in all these cell types, similar to mouse liver,
163 reversible reactions were closer to equilibrium compared to the irreversible reaction, PFK
164 (Fig. 1E). This result suggests that the thermodynamic characteristics in glycolysis are widely
165 conserved across species. An exception is PKLR, whose $\Delta_r G'$ in mouse liver was more than
166 20 kJ/mol smaller than those in the other cell types. Among the metabolite concentrations (or
167 ratios) involved in PKLR, pyruvate concentration and ATP/ADP were smaller in mouse liver
168 than in mammalian iBMK cells, yeast, and *E. coli* (Table S4). In particular, pyruvate
169 concentrations were two orders of magnitude smaller in mouse liver (3.77×10^{-2} mM)

170 compared to the other three cell types (5.88 mM in iBMK cells, 9.40 mM in yeast, and 3.66
171 mM in *E. coli*).
172

173 **$\Delta_r G'$ maintenance during fasting is associated with metabolite concentration**
174 **fluctuations in different ways among pathways**

175 To characterize the metabolic reactions exhibiting large thermodynamic changes
176 accompanying the fasting-induced metabolic shift, we linked the attributes of reactions
177 including reversibility and pathway to $\Delta_r G'_{16\mathrm{h}} - \Delta_r G'_{0\mathrm{h}}$, defined as $\Delta_r G'$ variations during
178 fasting (Fig. 2A). Among the seven irreversible reactions of glycolysis and gluconeogenesis,
179 four reactions (GCK, PFK, PKLR, and PC) exhibited an absolute $\Delta_r G'$ variation during
180 fasting greater than 5 kJ/mol. In contrast, only one reversible reaction (ALDO) out of 11
181 showed an absolute $\Delta_r G'$ variation during fasting exceeding 5 kJ/mol, despite the reversal
182 of reversible reaction directions between glycolysis and gluconeogenesis under these
183 conditions. This result suggests that reversible reactions maintained $\Delta_r G'$ more strictly than
184 irreversible reactions even though the sign of $\Delta_r G'$ is reversed. In the TCA cycle, the
185 absolute $\Delta_r G'$ variations during fasting were less than 3 kJ/mol for all reactions, indicating
186 that the TCA cycle is thermodynamically stable in response to fasting.

187

188 As $\Delta_r G'$ variations during fasting differed between irreversible and reversible reactions in
189 glycolysis and gluconeogenesis, we further examined the relationship between the distance
190 from equilibrium ($|\Delta_r G'|$) at *ad libitum* feeding and the absolute $\Delta_r G'$ variation (Fig. 2B).
191 In glycolysis and gluconeogenesis, the absolute $\Delta_r G'$ variations during fasting were less
192 than 3.5 kJ/mol for near-equilibrium reactions with $|\Delta_r G'| < 5$ kJ/mol at *ad libitum* feeding
193 except for PC. PC moved away from equilibrium only when gluconeogenesis is dominant in
194 response to fasting. In contrast, the absolute $\Delta_r G'$ variations of the reactions with $|\Delta_r G'| \geq$

195 5 kJ/mol at *ad libitum* feeding ranged between 0 and 10 kJ/mol, and were significantly larger
196 than those of the near-equilibrium reactions (p value = 0.037 < 0.05 calculated by two-tailed
197 Welch's *t*-test, n = 12 for near-equilibrium reactions with $|\Delta_r G'| < 5$ and n = 6 for the other
198 reactions with $|\Delta_r G'| \geq 5$ kJ/mol). This result suggests that $\Delta_r G'$ of near-equilibrium
199 reactions in glycolysis and gluconeogenesis tended to be strictly maintained, while this
200 tendency was lost among other reactions. In the TCA cycle, $\Delta_r G'$ was strictly maintained
201 regardless of the distance from equilibrium. The statistical test was not performed for the
202 TCA cycle due to a lack of near-equilibrium reactions.
203
204 To investigate the reason maintaining $\Delta_r G'$ in near-equilibrium reactions in glycolysis and
205 gluconeogenesis, as well as in the TCA cycle reactions, we compared the absolute $\Delta_r G'$
206 variation with the total absolute $\Delta_f G'$ variation of metabolites involved in the reaction (Fig.
207 2C). The total absolute $\Delta_f G'$ variation of metabolites is defined as $\sum\left|S\left(\Delta_f G'_{16\mathrm{h}} - \Delta_f G'_{0\mathrm{h}}\right)\right|$,
208 where *S* is the stoichiometric coefficient of a metabolite involved in the reaction. The $\Delta_r G'$
209 variation is associated in various ways with fluctuations in the $\Delta_f G'$ of substrates and
210 products, which depend on the metabolite concentrations. For example, when substrate and
211 product concentrations remain relatively constant and changes in their $\Delta_f G'$ remain small,
212 the $\Delta_r G'$ variation is small (*e.g.*, GPD in Fig. 2D). Even when substrate and product
213 concentrations largely fluctuate and changes in their $\Delta_f G'$ are large, the $\Delta_r G'$ variation can
214 remain small when the changes in $\Delta_f G'$ of substrate and products are cancelled out. This
215 can happen, for instance, when both the substrate and product $\Delta_f G'$ values increase

216 simultaneously (*e.g.*, GAPDH:PGK in Fig. 2D). In contrast, when the changes in $\Delta_f G'$ of
217 substrate and products are not cancelled out, the $\Delta_r G'$ variation becomes large (*e.g.*, GCK
218 in Fig. 2D). In glycolysis and gluconeogenesis, reactions with small absolute $\Delta_r G'$ variation
219 due to small fluctuation in metabolite concentrations, such as GPD, and due to the
220 cancellation of $\Delta_f G'$ variations such as GAPDH:PGK, were both observed (Fig. 2C). The
221 existence of the latter type of reaction suggests that while metabolite concentrations fluctuate
222 in response to fasting in glycolysis and gluconeogenesis, the fluctuations in metabolites
223 involved in near-equilibrium reactions were coordinated, thereby maintaining $\Delta_r G'$ of these
224 reactions. In the TCA cycle, the reason for maintaining the absolute $\Delta_r G'$ variations were
225 small fluctuations in metabolite concentrations for all the reactions.

226

227 **Thermodynamic Rate-limiting Candidates (TRCs) were maintained during fasting**

228 One of the physiological consequences of reaction distances from equilibrium is the control
229 of steady-state pathway fluxes. The extent to which perturbation of each reaction can control
230 pathway steady-state flux is quantified by the flux control coefficient (FCC) in metabolic
231 control analysis (MCA) [36,47]. In this study, we analytically calculated FCCs under both
232 arbitrary $\Delta_r G'$ landscapes and those observed in mouse liver within glycolysis (Fig. 3A),
233 gluconeogenesis (Fig. 3B), and the TCA cycle (Fig. 3C) from an enzymatic rate law using
234 the MCA's theorems. To incorporate reaction distance from equilibrium, we used reversible
235 kinetics called the direct binding modular rate law [48] as the enzymatic rate law. Under this
236 framework, a flux v can be decomposed into the effect of thermodynamics η_{rev} (Fig. 3D)
237 and substrate saturation $\eta_{\mathrm{sat,s}}$ [49]:

$$v = E k_{\mathrm{cat}}^{+} \eta_{\mathrm{rev}} \eta_{\mathrm{sat,s}}, \tag{3}$$

$$\eta_{\mathrm{rev}} = 1 - \exp\left(\frac{\Delta_r G'}{RT}\right), \tag{4}$$

$$\eta_{\mathrm{sat,s}} = \frac{\prod_{i \in M^{\mathrm{s}}} \left(\frac{c_i}{K_{\mathrm{m},i}}\right)^{|S_i|}}{1 + \prod_{i \in M^{\mathrm{s}}} \left(\frac{c_i}{K_{\mathrm{m},i}}\right)^{|S_i|} + \prod_{i \in M^{\mathrm{p}}} \left(\frac{c_i}{K_{\mathrm{m},i}}\right)^{|S_i|}} \tag{5}$$

238 where E is an enzyme concentration, k_{cat}^{+} is the forward catalytic constant, K_{m} is the
239 Michaelis-Menten constant, M^{s} is substrates, and M^{p} is products. Using this reaction rate
240 raw, we calculated FCC based on the connectivity theorem and summation theorem in MCA
241 [50] (see Methods). This FCC calculation depends on metabolite concentrations, $\Delta_f G'^{\circ}$, and
242 K_{m}. For $\Delta_f G'^{\circ}$, we used sampling values for the confidence interval calculation in GLEAM.

243 K_{m} values were sampled from distributions based on BRENDA database data [51]. Metabolite
244 concentrations were obtained by the following two approaches.
245
246 We investigated FCC for metabolite concentrations in mouse liver using sampled values for
247 confidence interval calculations in GLEAM, and FCC for arbitrary $\Delta_r G'$ landscapes to
248 identify thermodynamic conditions for large FCC. FCCs for arbitrary $\Delta_r G'$ landscapes
249 showed that FCC value larger than 0.5, which is greater than the sum of FCCs of the other
250 reactions in the pathway, required $\eta_{\mathrm{rev}} \approx 1$ except for in reactions located upstream in a
251 pathway (Fig. S1 A to D). In mouse liver, reactions with $\eta_{\mathrm{rev}} \approx 1$ at *ad libitum* feeding
252 included irreversible reactions GCK, PFK, PKLR, and the reversible reaction ALDO in
253 glycolysis. Among them, reactions that could achieve FCC ≈ 1 were GCK and PFK, while
254 the other reactions could achieve FCC of between 0.5 and 0.7 (Fig. 3E). We also found that
255 GPI, which is a reversible reaction located upstream in the pathway, could achieve FCC =
256 0.42 at $\eta_{\mathrm{rev}} \approx 0.70$. In gluconeogenesis, reactions with $\eta_{\mathrm{rev}} \approx 1$ after 16-hour fasting were
257 the irreversible reactions PC, PCK, FBP, and G6PC, all of which could achieve FCC ≈ 1 (Fig.
258 3F). All the other reactions exhibited only small FCC values. In the TCA cycle, similar FCC
259 distributions were observed at *ad libitum* feeding and after fasting (Fig. 3G, S3). Reactions
260 with $\eta_{\mathrm{rev}} \approx 1$ were irreversible reactions CS, ACO:IDH, OGDH, and a reversible reaction
261 LSC. Among these reactions, CS and OGDH could achieve FCC ≈ 1, while ACO:IDH and
262 LSC could achieve FCC slightly below 0.7. Generally, reversible reactions have not been
263 considered rate-limiting reactions because they have been recognized to be qualitatively
264 closer to equilibrium than irreversible reactions. However, our quantitative analysis

265 demonstrated that the reversible reactions GPI, ALDO, and LSC could achieve FCC of
266 between 0.4 and 0.7 comparable to several irreversible reactions. Considering the results of
267 arbitrary $\Delta_r G'$ landscapes, these large FCC values of the reversible reactions can be
268 attributed to GPI being located relatively upstream in glycolysis, and ALDO and LSC being
269 sufficiently away from equilibrium to exhibit $\eta_{\mathrm{rev}} \approx 1$ despite being closer to equilibrium
270 than irreversible reactions.
271
272 As described above, a reaction with FCC larger than 0.5 seems to be either away enough
273 from equilibrium to exhibit $\eta_{\mathrm{rev}} \approx 1$, or located upstream in a pathway. Because the location
274 of a reaction in a pathway depends on the definition of the pathway, a reaction being away
275 enough from equilibrium to exhibit $\eta_{\mathrm{rev}} \approx 1$ is a key determinant for the reaction to have
276 large FCC, sometimes being referred to as the rate-limiting step. Therefore, we introduced
277 Thermodynamic Rate-limiting Candidate (TRC) as reactions with $\eta_{\mathrm{rev}} \geq 0.86$
278 corresponding to $\Delta_r G' \leq -5$ kJ/mol, and examined which reaction is thermodynamically
279 capable of being a rate-limiting step for any pathway definitions at *ad libitum* feeding (Fig.
280 3H, 0h) and after fasting (Fig. 3H, 16h). TRC reactions both at *ad libitum* feeding and after
281 fasting included GCK, PFK, CS, and seven other reactions, indicating these reactions can be
282 a rate-limiting step regardless of fasting levels. The parameter η_{rev} and TRC status (either
283 TRC or not) are sensitive to $\Delta_r G'$ variations at a near-equilibrium region ($\Delta_r G' > -5$
284 kJ/mol) while they are insensitive at a far-from-equilibrium region ($\Delta_r G' < -10$ kJ/mol) (Fig.
285 3D). Due to this property, 15 out of 18 reactions remained either TRC (red line in Fig. 3H)
286 or non-TRC (blue line in Fig. 3H) across at *ad libitum* feeding and after fasting in glycolysis

287 and gluconeogenesis, where only $\Delta_r G'$ of near-equilibrium reactions were strictly
288 maintained. This result suggests that fasting-induced fluctuations in metabolite
289 concentrations occur within a range that maintains the TRC status for most reactions. The
290 three reactions of ALDO, PC, and PCK were the exceptions that did not remain TRC or non-
291 TRC (gray line in Fig. 3H), and whether these reactions are rate-limiting or not would depend
292 on fasting levels. The reactions maintaining their TRC status described above remain stable
293 across the threshold from η_{rev} = 0.73 to 0.99.
294

295 **Glycolysis and gluconeogenesis achieve efficient directional switching by expending**
296 **large Enzyme Costs**

297 A fundamental question in biology is to understand what biological systems are optimized
298 for. While objective functions optimized in microbial metabolism—such as maximizing
299 growth or ATP production [52] and minimizing enzyme demands [42]—have been reported, the
300 objective function for *in vivo* mammalian metabolism remains completely unknown.
301 Therefore, we examined the optimality of metabolism in mouse liver from the aspect of
302 metabolite concentrations and $\Delta_r G'$ landscape obtained from GLEAM.

303

304 By solving the equation of the direct binding modular rate law (Eq. 3) with respect to the
305 enzyme amount, we obtain

$$E = \frac{v}{k_{\mathrm{cat}}^{+}} \eta_{\mathrm{rev}}^{-1} \eta_{\mathrm{sat,s}}^{-1}. \quad (6)$$

306 This equation shows that the closer to a reaction is to equilibrium (the smaller η_{rev} is), the
307 greater the enzyme amount required to achieve the same flux v. Here we defined Enzyme
308 Cost (EC) as the product of enzyme amount and enzyme molecular weight, and Enzyme Cost
309 Minimum (ECM) as the theoretical state that minimizes the total EC within the entire
310 pathway (see Method). By comparing ECs and metabolite concentrations in mouse liver to
311 those in ECM, we investigated whether mouse liver metabolism is optimized for enzyme
312 demands reduction. As with FCC calculation, we calculated EC using sampling values of
313 metabolite concentrations and $\Delta_f G'^{\circ}$ used in the confidence interval calculation in GLEAM.
314 For K_{m} values, we obtained them as geometric means of data in the BRENDA database [51].

315

316 We calculated EC and ECM for the reactions in glycolysis at *ad libitum* feeding,
317 gluconeogenesis after 16-hour fasting, and the TCA cycle under both these conditions (Table
318 S5). The liver showed larger total EC compared to ECM, with a difference between pathways.
319 The liver/ECM ratio of total EC was on the order of 10^4 for glycolysis and gluconeogenesis,
320 but only 10^1 for the TCA cycle (Fig. 4A). Additionally, we compared ECM-predicted
321 metabolite concentrations with liver metabolite concentrations in each pathway, and found
322 typical fold errors of $10^{RMSE} = 29.79$ (RMSE: root mean square error on a $\log_{10}$-scale) for
323 glycolysis and gluconeogenesis and 14.40 for the TCA cycle (Fig. 4B). These findings show
324 that enzyme and metabolite concentrations in the liver are not optimized for EC, and this is
325 more evident in glycolysis and gluconeogenesis than in the TCA cycle.

326

327 To identify a key reaction contributing to the large total EC of glycolysis and gluconeogenesis
328 in mouse liver, we broke down the total EC of pathways into ECs of individual reactions
329 (Table S5). The GAPDH:PGK reaction in mouse liver exhibited the highest EC of 10^6 both
330 in glycolysis and gluconeogenesis (Fig. 4C), while EC of reactions in the TCA cycle (*e.g.*,
331 SDH, ACO:IDH, and FH) are at most on the order of 10^2. The EC values of GAPDH:PGK
332 are 99% and 89% of the total EC of glycolysis and gluconeogenesis, respectively, suggesting
333 that GAPDH:PGK outstandingly elevates the total EC of glycolysis and gluconeogenesis.
334 The high EC for GAPDH:PGK both in glycolysis and gluconeogenesis is attributed to two
335 factors. One factor is low substrate saturation (Fig. 4C, blue), which is given by the lower
336 substrate metabolite concentrations (3.4×10^{-3} mM of GAP *ad libitum* feeding and 1.3×10^{-2}

337 mM of 3PG after fasting) than their respective K_{m} values (1.9×10^{-1} mM for GAP and
338 3.5×10^{-1} mM for 3PG), resulting in large $\eta_{\mathrm{sat,s}}^{-1}$. From Eq. 6, a large $\eta_{\mathrm{sat,s}}^{-1}$, indicating low
339 substrate saturation, causes an increase in EC to carry a certain flux. Under this condition, an
340 increase in flux from higher enzyme levels is mitigated by fluctuations in metabolite
341 concentrations. The other factor of the high EC for GAPDH:PGK is liver thermodynamics
342 (Fig. 4C, red), where the reaction was markedly close to equilibrium ($\Delta_r G' = -0.01$ kJ/mol
343 both at *ad libitum* feeding and after fasting), leading to large η_{rev}^{-1}. When the reaction is close
344 to equilibrium, increasing the enzyme abundance enhances both the forward and reverse
345 fluxes, thus limiting the net flux increase. Thus, the elevated EC for this reaction is a result
346 of both low substrate saturation and high reaction reversibility.
347
348 The liver glycolysis and gluconeogenesis required much larger EC than ECM, especially in
349 the midstream reversible reactions due to large η_{rev}^{-1} values. We hypothesized that the reason
350 for this may be that the enzyme costs are required for enabling switching from glycolysis to
351 gluconeogenesis during fasting. To assess the metabolic hurdle for directional switching from
352 glycolysis to gluconeogenesis, we introduced the Metabolite Equilibrium Gap (MEG) as the
353 typical fold change in metabolite concentration required for the directional switching (Table
354 S6) (see Methods). In glycolysis and gluconeogenesis, mouse liver exhibited MEG = 1.35
355 while ECM exhibited MEG = 16.01 (Fig. 4D), suggesting that the liver achieves directional
356 switching from glycolysis to gluconeogenesis with much smaller metabolite concentration
357 changes than ECM. Unlike glycolysis and gluconeogenesis, the TCA cycle, which does not
358 undergo directional switching during fasting, exhibited a larger MEG (6.85) in the liver than

that of glycolysis and gluconeogenesis. The mouse liver expends a much larger enzyme cost in glycolysis and gluconeogenesis than the theoretical minimum, allowing it to achieve directional switching with smaller changes in metabolite concentration. Conversely, a smaller enzyme cost is expended for the TCA cycle—which does not undergo directional switching—than for glycolysis and gluconeogenesis.

365 **Robustness of $\Delta_r G'$ in the liver against obesity**

366 Obesity disrupts liver metabolism, leading to impaired homeostasis in response to fasting
367 [7,8,10] and subsequent development of various diseases [9,18–20]. Recent studies have reported
368 that the obesity-associated dysregulation of liver metabolism occurs even at *ad libitum*
369 feeding [11,12]. To reveal the impact of obesity-induced metabolic disruption on the
370 thermodynamic characteristics of reactions, we calculated $\Delta_r G'$ in the *ob*/*ob* mouse liver
371 during fasting.

372

373 The $\Delta_r G'$ landscape in *ob*/*ob* mouse liver (Fig. 5A; Table S2) showed that the difference in
374 $\Delta_r G'$ from WT mouse liver was less than 5 kJ/mol for most reactions both at *ad libitum*
375 feeding and after 16-hour fasting (Fig. 5B, C, S3). Consequently, the overall trend of
376 irreversible reactions being far from equilibrium ($\Delta_r G' < -10$ kJ/mol) and reversible
377 reactions being near equilibrium ($\Delta_r G' > -5$ kJ/mol) was preserved even under obesity. The
378 similar $\Delta_r G'$ values between WT and *ob*/*ob* mouse indicate that the concentration ratios of
379 substrates and products for the reactions are comparable between the genotypes. Individual
380 metabolite concentrations (Table S2), however, showed discrepancies between WT and *ob*/*ob*
381 mouse liver (Fig. 5D), with log2 fold change exceeding 0.5 for 16/31 and 13/31 metabolite
382 concentrations at *ad libitum* feeding and after 16-hour fasting, respectively. This result
383 suggests that the thermodynamic characteristics of reactions remain robust against obesity
384 despite the changes in individual concentrations. Particularly, in most reversible reactions of
385 glycolysis and gluconeogenesis, the differences in $\Delta_f G'$ between WT and *ob*/*ob* mouse were
386 not reflected in the differences in $\Delta_r G'$ (Fig. 5E). This result prominently demonstrates that

387 the reaction thermodynamic characteristics are robust to obesity while the individual
388 metabolite concentrations are sensitive.
389

390 **DISCUSSION**

391 We revealed the $\Delta_r G'$ landscape of glucose metabolism in *in vivo* mouse liver for the first
392 time from fasting time-series absolute quantitative metabolome data using the newly
393 developed GLEAM. In mouse liver, overall trend of $\Delta_r G'$ landscape was maintained
394 regardless of fasting level (Fig. 1B, C). The $\Delta_r G'$ maintenance was markedly strict in near-
395 equilibrium reactions in glycolysis and gluconeogenesis such as GAPDH:PGK (Fig. 2B),
396 despite large fluctuations in metabolite concentrations (Fig. 1D, 2C), while this strictness was
397 not true for the other reactions such as GCK. In the TCA cycle, overall $\Delta_r G'$ variations were
398 small due to minimal metabolite concentration fluctuations during fasting (Fig. 2B, C). This
399 thermodynamic robustness against fasting led to maintenance of the reactions that could have
400 large FCC *i.e.*, TRC during fasting (Fig. 3H) because FCC is sensitive to $\Delta_r G'$ variation
401 only in the near-equilibrium region. The thermodynamic landscape in the liver could also
402 contribute to an efficient switching from glycolysis to gluconeogenesis by expending a larger
403 enzyme expression than that theoretically minimized (Fig. 4A to D). We also found similar
404 $\Delta_r G'$ landscapes between WT and *ob*/*ob* mouse (Fig. 5A to C), while metabolite
405 concentrations were quite different (Fig. 5D). Our results revealed that the liver robustly
406 maintains $\Delta_r G'$ landscapes favorable for metabolic control in contrast to fluctuations in
407 individual metabolite concentrations caused by fasting and obesity.

408

409 Methods for estimating thermodynamically consistent metabolite concentrations, $\Delta_f G'^{\circ}$, and
410 $\Delta_r G'$ from absolute quantitative metabolome data have been proposed in previous studies
411 [26,27,53]. In these methods, $\Delta_f G'^{\circ}$ values were fixed to the inputs of the model, or estimated

412 without considering the covariance. However, metabolites sharing common chemical groups,
413 such as ADP and ATP, tend to exhibit similar $\Delta_f G'^{\circ}$ values, because $\Delta_f G'^{\circ}$ depends on
414 structures of metabolites. Incorporating covariance information into the estimation thus
415 better reflects the underlying chemical relationships between metabolites and allows for
416 narrower confidence intervals in the estimated values [54]. By leveraging the covariance matrix
417 of $\Delta_f G'^{\circ}$ from eQuilibrator [55], GLEAM achieves more precise and consistent estimation of
418 thermodynamic characteristics throughout the entire metabolic network.
419
420 Our study narrowed down the reactions that could achieve large FCC in the pathways, *i.e.*,
421 candidates for a rete-limiting step using the obtained $\Delta_r G'$ landscape in mouse liver (Fig.
422 3E to G, S2). A previous study experimentally measured FCC in glycolysis in iBMK cells,
423 and reactions exhibiting large FCCs are hexokinase (HK), which catalyzes the same reaction
424 as GCK, and PFK [56]. Another previous study exhibited PC having dominant FCC in
425 gluconeogenesis in rat liver [57,58]. Although no studies have measured FCC in the TCA cycle
426 to our knowledge, CS, IDH, and OGDH have conventionally been regarded as rate-limiting
427 steps. All these reactions are included in the TRCs in this study, supporting the validity of
428 our $\Delta_r G'$ estimation even though this study focuses on mouse liver metabolism. While one
429 study based on standard-state calculation has indirectly showed the connection between
430 reactions away from equilibrium and driver nodes to control the entire network defined using
431 control theory in terms of topological features [59], the functional advantage of controlling
432 pathway flux via these reactions remains unclear and is an important future topic for
433 understanding system-level metabolic regulation.

When calculating EC, we made two assumptions: having common turnover number, k_{cat} values for all reactions and setting saturation (c/K_{m}) to the geometric mean of the pathway when K_{m} could not be obtained from BRENDA. These assumptions were required because of the difficulty of obtaining kinetic parameters in mammals. The former assumption may cause inaccurate weighting of individual enzymes in the total EC minimization, and the latter may lead to inaccurate $\eta_{\mathrm{sat,s}}^{-1}$. However, the metabolite concentrations close to ECM were reported with a modeling where k_{cat} and K_{m} information was lacking and only the influence of η_{rev}^{-1} was considered [42]. This means that the $\Delta_r G'$ landscape in ECM would be similar under any k_{cat} and K_{m} values. Therefore, our conclusion of mouse liver metabolism not being optimized for enzyme cost reduction would be reasonable regardless of k_{cat} and K_{m} assumptions.

According to Eq. 23, 24, 30 to 35, and 38, the design of $\Delta_r G'$ landscape faces a trade-off between FCC concentration and enzyme cost minimization. If only a few reactions in a metabolic pathway are far from equilibrium and exhibit η_{rev} close to 1, large FCCs are likely to be concentrated in these reactions. In this case, η_{rev} of other reactions are close to zero, leading to a large EC. This trade-off can be rephrased as a trade-off between flexibility responding to multiple conditions and survival cost reduction under a single condition because the pathway flux can be efficiently regulated through a minimal number of enzyme activity changes when FCCs are concentrated in limited reactions. A similar trade-off also occurs between MEG reduction and enzyme cost minimization. In mouse liver, particularly

456 in glycolysis and gluconeogenesis, reactions that could achieve high FCC were concentrated
457 in a few reactions (Fig. 3E to G, S2), and MEG was remarkably small (Fig. 4D), while there
458 were large deviations between mouse liver and ECM in total EC and metabolite
459 concentrations (Fig. 4A, B). These results indicate that metabolic regulation in mouse liver
460 adopts a strategy of flexibly responding to changes in environmental and physiological
461 conditions rather than optimizing for a certain condition. In contrast, the previous study in *E.*
462 *coli* showed that both enzyme concentrations and metabolite concentrations are well
463 predicted by ECM within a typical fold error range of 10^0 [42] (Fig. S3). Taken together, these
464 facts suggest differences in metabolic regulation strategies between cell types; mouse liver
465 expends costs to perform flexible metabolic regulation, while *E. coli* optimized survival cost
466 in a certain condition. Furthermore, our study also showed that this difference in metabolic
467 regulation strategy may also exist between pathways by demonstrating the large differences
468 in TRC proportions and total EC optimality between glycolysis and gluconeogenesis, and the
469 TCA cycle. Note that although glycolysis in mouse liver and *E. coli* shared a common
470 thermodynamic tendency of reversible reactions being close to equilibrium with $\Delta_r G' < -10$
471 kJ/mol (Fig. 1E), EC in them can be greatly different. As shown in Eq. 38 and 39, thermoduric
472 characteristics of reactions affect EC through η_{rev}^{-1}, which indicates $v^{\mathrm{total}}/v^{\mathrm{net}}$, where
473 v^{total} is the total flux of forward and backward reactions, and v^{tatal} is the net flux. In *E.*
474 *coli*, most reversible reactions exhibited $\Delta_r G' < -1$ kJ/mol, contributing to reducing EC
475 with η_{rev}^{-1} on the order of 10^0 (Fig. S4, orange) [26,60]. In contrast, most reversible reactions in
476 mouse liver exhibited $\Delta_r G' > -0.1$ kJ/mol, where η_{rev}^{-1} rises sharply (Fig. S4, green),
477 leading to much larger EC than *E. coli*.

One of the limitations of this study is that we assumed hepatocytes as a single compartment and calculated $\Delta_r G'$ from metabolite concentrations averaged within the cell. As glycolysis operates in the cytosol and the TCA cycle operates in mitochondria, more accurate $\Delta_r G'$ calculation requires concentrations in each of these compartments. Furthermore, localized concentrations can be affected by substrate channeling [61]. Substrate channeling is a phenomenon where enzymes of consecutive reactions form complexes, allowing the product of the former enzyme to be directly transferred to the active site of the latter enzyme without being released into the solvent. For reactions involved in substrate channeling, $\Delta_r G'$ is dependent on the channeled metabolite concentration in a limited space among the enzymes. Although substrate channeling has not yet been confirmed in living organisms, the channeling of oxaloacetate between MDH and CS has been indirectly supported by experiments [62,63], and ALDO, TPI, and GAP have also been suggested to form complexes [64,65]. Another limitation is that the FCC calculations were based solely on stoichiometric relationships and did not account for allosteric regulations because of the severe lack of K_{i} in mammals and simplification of the calculation. Inclusion of allosteric regulations would alter FCC values, allowing for further narrowing down the reactions that can have a large FCC.

In conclusion, we developed GLEAM to estimate $\Delta_r G'$ in the glucose metabolism in mouse liver and revealed the thermodynamic robustness against fasting and obesity. Furthermore, we suggested that these thermodynamic characteristics in the liver contribute to efficient

500 metabolic control in two ways: the maintenance of rate-limiting step candidates and the
501 switching between glycolysis and gluconeogenesis with minimal metabolite fluctuations by
502 expending large enzyme expressions. This study thus provides crucial insights into the
503 principles underlying the highly flexible and robust metabolic regulation observed in
504 mammalian liver, paving the way for future investigations into therapeutic targets for
505 metabolic diseases.
506

RESOURCE AVAILABILITY

LEAD CONTACT

Requests for further information and resources should be directed to and will be fulfilled by the lead contact, Shinya Kuroda (skuroda@bs.s.u-tokyo.ac.jp).

MATERIAL AVAILABILITY

This study did not generate new unique reagents.

DATA AND CODE AVAILABILITY

Metabolomic data from WT and *ob*/*ob* mice in our previous studies [8,66] were used in this study.

The information on kinetic parameter (Michaelis-Menten constant and turnover number) distributions used for FCC calculation, the FCC values generated in this study, and the MATLAB code for GLEAM and the analysis of FCC and EC are deposited in GitHub (https://github.com/tabekawa/Thermodynamics_MouseLiver). All other data needed to evaluate the conclusions in the paper are present in the paper or the supplemental information.

Any additional information required to reanalyze the data reported in this paper is available from the lead contact upon request.

ACKNOWLEDGMENTS

We thank our laboratory members for critically reading this manuscript. The computational analysis of this work was performed in part with support of the supercomputer system of the National Institute of Genetics (NIG), Research Organization of Information and Systems (ROIS).

This study was supported by the Japan Society for the Promotion of Science (JSPS) KAKENHI (Grant Numbers JP17H06300, JP17H06299, JP18H03979, JP21H04759, JP22K17992, JP23H04946, JP23H04939) (S.K.); the Japan Science and Technology Agency (JST) as part of CREST (JPMJCR2123, JPMJCR25T3) and as part of ASPIRE (JPMJAP24B1) (S.K.); The Uehara Memorial Foundation (S.K.); AMED Grant Number JP21zf0127001 (T.S.); JST, CREST Grant Number JPMJCR2123 (T.S.); MEXT KAKENHI Grant Number JP23H04946 (T.S.); World Premier International Research Center Initiative (WPI), Human Biology-Microbiome-Quantum Research Center (Bio2Q), MEXT, Japan (T.S.); JSPS KAKENHI JP24K11417 (A.H.); and the FOREST Program of the Japan Science and Technology Agency (JPMJFR2052) (A.H.).

AUTHOR CONTRIBUTIONS

Conceptualization: T.A., S.O., and S.K.

Methodology: T.A., S.O., A.H., and T.S.

Investigation: T.A., A.H., and T.S.

Visualization: T.A.

Funding acquisition: A.H., T.S., and S.K.

Project administration: S.K.

Supervision: S.K.

Writing – original draft: T.A., S.O., and S.K.

Writing – review & editing: T.A., S.O., A.H., T.S., and S.K.

DECLARATION OF INTERESTS

The authors declare no competing interests.

DECLARATION OF GENERATIVE AI AND AI-ASSISTED TECHNOLOGIES

During the preparation of this work, the authors used ChatGPT, DeepL, and Claude in order improve the readability and language of the manuscript. After using these tools, the authors reviewed and edited the content as needed and take full responsibility for the content of the publication.

565 **STAR METHODS**

566 **EXPERIMENTAL MODEL AND PARTICIPANT DETAILS**

567 Metabolomic data from WT and *ob*/*ob* mice in our previous studies [8,66] were used in this
568 study.

569

570 **METHOD DETAILS**

571 **Metabolic network for glucose metabolism in mice**

572 A metabolic network for glucose metabolism in mice was constructed to calculate $\Delta_r G'$. The
573 network consists of total 55 reactions and 80 metabolites in the liver, muscle, and blood (the
574 same reactions and metabolites in different compartments were counted as distinct ones), and
575 involves glycolysis, gluconeogenesis, TCA cycle, glycogen metabolism, alanine metabolism,
576 and transporters (Fig. S5, Table S3). Among the 55 reactions, we defined 23 reversible
577 reactions and 32 irreversible reactions based on the tissue-specific genome-scale metabolic
578 network [67]. All the transporters were defined as reversible reactions.

579

580 Reversible reactions GAPDH and PGK were combined into a single reversible reaction
581 GAPDH:PGK because 1,3-bisphosphoglycerate was not measured in the metabolomic data
582 [8]. According to the experimentally measured metabolite concentrations, a reversible reaction
583 ACO proceeded in the reverse direction of the oxidative TCA cycle with a little
584 thermodynamic driving force at all the time points in WT and *ob*/*ob* mice, breaking a
585 sequential pathway from CS to FH. Since this long sequential pathway is necessary for the
586 downstream analysis, such as FCC and MEC calculation, we summed ACO and irreversible

587 reaction, IDH, which have a large thermodynamic driving force in the direction of the
588 oxidative TCA cycle, as a single irreversible reaction, ACO:IDH.
589
590 In the skeletal muscle, FBP, G6PC, and PCK in gluconeogenesis were not included in the
591 metabolic network. Although PC is also involved in gluconeogenesis, PC is included in the
592 metabolic network of skeletal muscle because we could not exclude the possibility of its
593 expression in the skeletal muscle [68,69].
594
595 In this study, we assumed the liver and skeletal muscle as a single compartment of
596 hepatocytes and myocytes, respectively, and cytosolic and mitochondrial compartments in
597 these cells were not considered for simplification of the modeling. Therefore, the $\Delta_r G'$
598 calculated in this study represents the average values within the cells.
599
600 **Algorithm of GLEAM**
601 We developed GLEAM as a method to estimate complete set of thermodynamically
602 consistent metabolite concentrations and $\Delta_f G'^{\circ}$ values, from metabolomic data on a
603 logarithmic scale, $\mathbf{ln}\,\boldsymbol{c} \in \mathbb{R}^{m \times h \times g}$, and $\Delta_f G'^{\circ}$ data calculated by the component
604 contribution method [70], $\boldsymbol{\Delta_f G'^{\circ}} \in \mathbb{R}^{m}$, where m, h, g are the number of metabolites,
605 timepoints, and genotypes, respectively. Since metabolomic and $\Delta_f G'^{\circ}$ data contain
606 uncertainties and missing values, directly substituting them into the definition equation of
607 $\Delta_r G'$ (Eq. 1, 2) often violates the second law of thermodynamics. To address this issue,

GLEAM corrects for the uncertainties and missing values by calculate the most plausible values based on measured metabolomic data within a thermodynamically feasible space.

We first formulate the quadratic programming problem to minimize the departures of estimated metabolite concentrations and $\Delta_f G'^{\circ}$ from the experimental and database values under thermodynamic and physiological constraints:

$$\min_{y \in \{\ln c, \Delta_f G'^{\circ}\}, a} Z_{\mathrm{QP}}$$

$$= \sum_{y} \frac{1}{\# y^{\mathrm{exp}}} \left\{ (\boldsymbol{y} + \boldsymbol{a} - \boldsymbol{y}^{\mathbf{exp}})^{\mathrm{T}} \boldsymbol{\Sigma}_{(y)}^{-1} (\boldsymbol{y} + \boldsymbol{a} - \boldsymbol{y}^{\mathbf{exp}}) + \sum_{i} \lambda \left| \frac{(\boldsymbol{P}_i)^{\mathrm{T}} \boldsymbol{a}}{\sqrt{D_{ii}}} \right| \right\}$$

$$\text{s.t.} \qquad \Delta_r G'_j < 0 \quad \forall i \in M, \forall j \in N$$

$$\Delta_r G'_j = \sum_{i \in M} S_{i,j} \left(\Delta_f G'^{\circ}_i + RT \ln c_i \right) \quad \forall j \in N^{\mathrm{cell}}$$

$$\Delta_r G'_{\mathrm{GLUT}} = RT \ln \frac{[\mathrm{Glu[h]}]}{[\mathrm{Glu[b]}]} \tag{7}$$

$$\Delta_r G'_{\mathrm{MCT}} = RT \ln \frac{[\mathrm{H^+[b]}][\mathrm{Lac[b]}]}{[\mathrm{H^+[h]}][\mathrm{Lac[h]}]}$$

$$b_i \leq \ln c_i \leq ub_i \quad \forall i \in M$$

$$b_i \leq \ln \frac{c_{i_1}}{c_{i_2}} \leq ub_i \quad \forall (i_1, i_2) \in M^{\mathrm{cofactor}}$$

where c_i is concentration of metabolite i, S_{ij} is stoichiometric coefficient of metabolite i in reaction j, R is gas constant, and T is temperature. M, N, and N^{cell} are sets of metabolites, reactions, and intracellular reactions, respectively. M^{cofactor} is the cofactor pairs of which the ratio was constrained. $\boldsymbol{\Sigma}$ is variance-covariance matrix of which the eigen decomposition is $\boldsymbol{\Sigma} = \mathbf{PDP}^{\mathrm{T}}$. a is systematic error, and λ is regularization parameter. The

superscript exp means measured or database value. The first term in curly brackets of the objective function represents the variance and covariance-weighted residuals of estimated metabolite concentrations and $\Delta_f G'^{\circ}$, which considers systematic errors from experimental operations, while the second term represents a regularization term for systematic errors to avoid overfitting. By using the covariances in $\Delta_f G'^{\circ}$ for the weight of residuals, the estimation reflects the correlations in $\Delta_f G'^{\circ}$ due to shared chemical groups. In contrast, all covariances between metabolite concentrations were set to zero, making $\boldsymbol{\Sigma}$ a diagonal matrix, since no prior correlation in metabolite concentrations is expected.

The solution of the optimization problem (7) may not provide unique concentrations, especially for unmeasured metabolites, which can lead to undetermined $\Delta_r G'$ of the reactions involving the unmeasured metabolites. To estimate unique $\Delta_r G'$, two terms with variance of unmeasured metabolite concentrations were added to the objective function:

$$\begin{aligned} Z_{\mathrm{QP_unique}}(y,a) = &\sum_{y} \frac{1}{\#y^{\mathrm{exp}}} \left\{ (\boldsymbol{y}+\boldsymbol{a}-\boldsymbol{y}^{\mathbf{exp}})^{\mathrm{T}} \boldsymbol{\Sigma}_{(y)}^{-1} (\boldsymbol{y}+\boldsymbol{a}-\boldsymbol{y}^{\mathbf{exp}}) + \sum_{i} \lambda \left| \frac{(\boldsymbol{P}_i)^{\mathrm{T}} \boldsymbol{a}}{\sqrt{D_{ii}}} \right| \right\} \\ &+ \epsilon_1 \sum_{(h_1,h_2)\in H^{\mathrm{adj}}} \frac{1}{(h_2-h_1)} \sum_{i\in M^{\mathrm{unmeasured}}} \left(\ln c_{i,h_2} - \ln c_{i,h_1}\right)^2 \\ &+ \epsilon_2 \sum\nolimits_{i\in M^{\mathrm{unmeasured}}} \left(\ln c_i - \widehat{\ln c_i}\right)^2 \end{aligned} \tag{8}$$

where H^{adj} is pairs of adjacent timepoints, $M^{\mathrm{unmeasured}}$ is unmeasured metabolites, $\widehat{\ln c}$ is median of upper and lower bounds of metabolite concentration, and ϵ_1 is small values enough to prioritize the first term over the second term. Similarly, ϵ_2 ($\epsilon_1 \gg \epsilon_2$) allows the second term to take precedence over the third term. The second term of the objective function

636 (the first additional term) reduces the sum of concentration changes of unmeasured
637 metabolites across time points, making smooth concentration changes more likely to be
638 estimated than unnatural repetition of increases and decreases. The third term of the objective
639 function (the second additional term) departures of the estimated unmeasured metabolite
640 concentrations from the median of their upper and lower bounds. This term can be justified
641 by the trade-off in increasing concentrations between elevation of enzyme efficiency and
642 cellular burden from osmotic pressure and toxicity [40,71]. Since the objective function includes
643 terms with greatly different orders of magnitude due to $\epsilon \in \{\epsilon_1, \epsilon_2\}$, it has difficulty in
644 optimized at once. Therefore, in implementation, we first solve the optimization problem
645 only for the first term, then, with the measured metabolite concentrations and $\Delta_f G'^{\circ}$ fixed
646 to the obtained solutions, and then solve the optimization problem for the second and third
647 terms.
648
649 Metabolic networks can include reversible reactions and their directions are unknown under
650 a condition of interest. By introducing binary variables representing reaction, GLEAM model
651 is finally formalized by the following mixed integer quadratic programming problem:
652

$$\min_{y\in\{\ln c,\Delta_f G'^{\circ}\},a,v,d} Z_{\mathrm{MIQP}}$$

$$= \sum_{y} \frac{1}{\#y^{\exp}} \left\{ (\boldsymbol{y}+\boldsymbol{a}-\boldsymbol{y}^{\mathbf{exp}})^{\mathrm{T}} \boldsymbol{\Sigma}_{(y)}^{-1} (\boldsymbol{y}+\boldsymbol{a}-\boldsymbol{y}^{\mathbf{exp}}) + \sum_{i} \lambda \left| \frac{(\boldsymbol{P_i})^{\mathrm{T}} \boldsymbol{a}}{\sqrt{D_{ii}}} \right| \right\}$$

$$+ \epsilon_1 \sum_{(h_1,h_2)\in H^{\mathrm{adj}}} \frac{1}{(h_2-h_1)} \sum_{i\in M^{\mathrm{unmeasured}}} \left(\ln c_{i,h_2} - \ln c_{i,h_1}\right)^2$$

$$+ \epsilon_2 \sum\nolimits_{i\in M^{\mathrm{unmeasured}}} \left(\ln c_i - \widehat{\ln c_i}\right)^2$$

$$\text{s.t.} \qquad d_j \cdot \Delta_r G'_j < 0 \quad \forall i \in M, \forall j \in N$$

$$\Delta_r G'_j = \sum_{i\in M} S_{i,j}\left(\Delta_f G'^{\circ}_i + RT \ln c_i\right) < 0 \quad \forall i \in M, \forall j \in N^{\mathrm{cell}}$$

$$\Delta_r G'_{\mathrm{GLUT}} = RT \ln \frac{[\mathrm{Glu[h]}]}{[\mathrm{Glu[b]}]}$$

$$\Delta_r G'_{\mathrm{MCT}} = RT \ln \frac{[\mathrm{H^+[b]}][\mathrm{Lac[b]}]}{[\mathrm{H^+[h]}][\mathrm{Lac[h]}]} \tag{9}$$

$$d_j \in \{-1,1\} \quad \forall j \in N^{\mathrm{rev}}$$

$$d_j \in \{1\} \quad \forall j \in N^{\mathrm{irrev_f}}$$

$$d_j \in \{-1\} \quad \forall j \in N^{\mathrm{irrev_b}}$$

$$d_j \cdot v_j > 0 \quad j \in N$$

$$\sum_{j\in N} S_{i,j} v_j = 0 \quad i \in M^{\mathrm{steady}}$$

$$lb_i \le \ln c_i \le ub_i \quad \forall i \in M$$

$$lb_i \le \ln \frac{c_{i_1}}{c_{i_2}} \le ub_i \quad \forall (i_1, i_2) \in M^{\mathrm{cofactor}}$$

where v_j is metabolic flux through reaction j, $d_j = \{1, -1\}$ is a binary variable representing direction of reaction j, and N^{rev} is reversible reactions. $N^{\mathrm{irrev_f}}$ and $N^{\mathrm{irrev_b}}$ are irreversible reactions of which the direction is fixed to forward and backward with respect to the definition of metabolic network, respectively. M^{steady} is metabolites assumed to be in steady state. To solve this mixed integer quadratic programming problem efficiently, GLEAM treats it as a bilevel optimization problem, where the optimization of binary variables is the upper-level problem and the optimization of continuous variables is the lower-level problem:

$$\begin{aligned} \min_{d} \quad & Z_{\mathrm{MIQP}}\,(y^*, a^*, v^*, d) \\ \text{s.t.} \quad & y^*, a^*, v^* \in \arg\min_{y,a,v} Z_{\mathrm{MIQP}}(y, a, v, d) \\ & y, a, v, d \in \Omega_{\mathrm{GLEAM}} \end{aligned} \tag{10}$$

where Ω_{GLEAM} is the solution space defined in the problem (9). In the bilevel optimization problem, binary variables are optimized by a genetic algorithm, while continuous variables are optimized by the interior-point method under the individuals of binary variables (Fig. S6). The genetic algorithm was performed by the MATLAB function ga with termination condition of FunctionTolerance = 10^{-9} and population size of PopulationSize = 500. The lower-level quadratic programming problem was solved using Gurobi [72] MATLAB API with dual feasibility tolerance of OptimalityTol = 10^{-9} and primal feasibility tolerance of FeasibilityTol = 10^{-9}. This bilevel optimization was performed 10 times from random initial values, and the solution with the minimum objective function value was selected as the optimal solution.

Calculation of confidence intervals

The confidence intervals of the estimation by GLEAM were calculated using parametric bootstrap sampling of metabolite concentrations and $\Delta_f G'^{\circ}$. These data were first resampled by adding perturbation based on the variance and residual of each metabolite concentration and $\Delta_f G'^{\circ}$ in the $\Delta_r G'$ estimation by Eq. 9 using the experimental and database values [27,73]. To generate $\Delta_f G'^{\circ}$ samples reflecting their covariance, the perturbations were applied after the basis of $\Delta_f G'^{\circ}$ vector was transformed by transposed matrix of the eigenvectors of the variance-covariance matrix:

$$\ln c_i^b = \ln c_i^{\exp} + \sigma_i \delta_i^b, \quad \forall b \in B, \tag{11}$$

$$\left(\boldsymbol{P}_{(\Delta_f \boldsymbol{G}'^{\circ})\boldsymbol{i}}\right)^{\mathrm{T}} \boldsymbol{\Delta_f G'^{o,b}} = \left(\boldsymbol{P}_{(\Delta_f \boldsymbol{G}'^{\circ})\boldsymbol{i}}\right)^{\mathrm{T}} \boldsymbol{\Delta_f G'^{o,\exp}} + \sqrt{D_{(\Delta_f G'^{o})ii}}\,\delta_i^b, \tag{12}$$

$$\boldsymbol{\Sigma}_{(\boldsymbol{y})}^{\boldsymbol{b}} = \boldsymbol{\Sigma}_{(\boldsymbol{y})}, \tag{13}$$

$$\delta_i^b \sim \mathcal{N}(0, (sd^*)^2), \tag{14}$$

$$sd^* = \sqrt{\frac{1}{\#y^{\exp} - 1} \sum_i \left(\frac{\left(\boldsymbol{P}_{(y)\boldsymbol{i}}\right)^{\mathrm{T}} \boldsymbol{y}^* + \left(\boldsymbol{P}_{(y)\boldsymbol{i}}\right)^{\mathrm{T}} \boldsymbol{a}^* - \left(\boldsymbol{P}_{(y)\boldsymbol{i}}\right)^{\mathrm{T}} \boldsymbol{y}^{\mathbf{exp}}}{\sqrt{D_{(y)ii}}} - err^* \right)^2}, \tag{15}$$

$$err^* = \frac{1}{\#y^{\exp}} (\boldsymbol{y}^* + \boldsymbol{a}^* - \boldsymbol{y}^{\mathbf{exp}})^{\mathrm{T}} \boldsymbol{\Sigma}_{(y)}^{-1} (\boldsymbol{y}^* + \boldsymbol{a}^* - \boldsymbol{y}^{\mathbf{exp}}) \tag{16}$$

where b is the indices of bootstrap samples B, $*$ represents the optimized values by Eq. 9 using the experimental and database values. δ is gaussian noise generated from the normal distribution with mean 0 and standard deviation sd^*, which represents the standard deviation of metabolite concentration and $\Delta_f G'^{\circ}$ residuals in the $\Delta_r G'$ estimation from the

experimental and database values. Using the resampled metabolite concentrations and $\Delta_f G'^{\circ}$ values, we conducted the estimation of thermodynamically consistent metabolite concentrations and $\Delta_f G'^{\circ}$ in the same manner as the estimation from the experimental and database values. In this optimization, the directions of reversible reactions were fixed to those estimated from the experimental and database values. This resampling and optimization were performed 2000 times. By applying the percentile method to the resulting 2000 sets of the estimated values, we obtained the 95% confidence intervals.

Selection of regularization parameter

The regularization parameter λ for systematic errors in GLEAM was selected by the reduced chi-square (χ^2_{red}). χ^2_{red} was calculated using the estimated metabolite concentrations and $\Delta_f G'^{\circ}$ from resampled values [27,73]:

$$\chi^2_{\mathrm{red}} = \frac{\#y^{\mathrm{exp}} EPE}{df}, \tag{17}$$

$$EPE = \frac{1}{\#B} \sum_{b \in B} \frac{1}{\#y^{\mathrm{exp}}} \left(\boldsymbol{y}^{b*} + \boldsymbol{a}^{b*} - \boldsymbol{y}^{\mathbf{exp}}\right)^{\mathrm{T}} \boldsymbol{\Sigma}_{(y)}^{-1} \left(\boldsymbol{y}^{b*} + \boldsymbol{a}^{b*} - \boldsymbol{y}^{\mathbf{exp}}\right), \tag{18}$$

$$df = \frac{\#y^{\mathrm{exp}}}{2sd^*} (EPE - err^*) \tag{19}$$

where $b*$ represents the optimized values calculated from the resampled values. The model is interpreted as fitting the data ideally when χ^2_{red} = 1, as overfitting when χ^2_{red} < 1, and as poorly fitting when χ^2_{red} > 1. In this study, χ^2_{red} = 1.03 when λ = 1.51, and therefore it was selected as the best regularization parameter.

701 **Application of GLEAM to mice data**

702 We applied GLEAM to absolute quantitative metabolome data in the liver, skeletal muscle,
703 and plasma from WT and *ob*/*ob* mice (n = 5) after 0, 2, 4, 6, 8, 12, and 16 hours of fasting
704 (Table S1), which were measured in our previous studies [8,66]. We used the logarithmic mean
705 and variance of the metabolites, which were successfully measured in three or more samples
706 per condition, and metabolites with two or fewer measured samples were treated as
707 unmeasured metabolites. The cofactors ATP, ADP, GTP, GDP, NAD^+, NADH, FAD, FADH2,
708 $NADP^+$, and NADPH were treated as unmeasured metabolites regardless of the number of
709 measured samples due to sample degradation, and instead, their ratios were constrained by
710 previous reports (Table S7). Intracellular lactate was also treated as an unmeasured
711 metabolite in the same manner as the cofactors because it might leach out of the container
712 during measurement. The upper and lower bounds for many metabolites in GLEAM were set
713 to a physiologically typical range of intracellular metabolite concentration (lower bound: 10^{-}
714 ^{7} M, upper bound: 10^{-2} M) [26], while the bounds for some unmeasured metabolites were
715 individually defined based on biological knowledge (Table S7).

716

717 $\Delta_f G'^{\circ}$ data calculated by the component contribution method [70] were retrieved from
718 eQuilibrator database (Table S1) [55]. We used the identical $\Delta_f G'^{\circ}$ data for both liver and
719 skeletal muscle under the condition in eQulibrator of pH = 7.2, pMg = 3.0, and ionic strength
720 = 0.15 M [26]. We also set the condition in blood to pH = 7.4 [74] because $\Delta_r G'$ for MCT depends
721 on pH in the cells and blood. Temperature was input to T = 310.15 K for all the
722 compartments.

723

724 In the liver, glycolysis was assumed to be dominant at the 0h-fasting state (*ad libitum* feeding)
725 while gluconeogenesis was assumed to take over after no later than 16h-fasting, both in WT
726 [75–79] and *ob*/*ob* mouse [80]. At these two timepoints, the directions of reversible reactions
727 involved in glycolysis and gluconeogenesis (GPI, ALDO, TPI, GAPDH:PGK, PGAM, ENO,
728 PGM, GPD, LDH) were fixed and treated as those of the irreversible reactions in the
729 calculation of GLEAM.

730

731 Since the reaction rates are sufficiently faster than the temporal changes in metabolite and
732 enzyme levels during starvation, our metabolic model was assumed to be in a pseudo-steady
733 state at each measured time point. This assumption leads to mass balance equilibrium for the
734 intermediate metabolites (G6P, F6P, F1,6BP, DHAP, GAP, 3PG, 2PG, PEP, Pyruvate, AcCoA,
735 Cit, Isocit, AKG, SucCoA, Suc, Fum, Mal, OAA) within the metabolic network.

736

737 **Derivation of FCC**

738 We derived flux control coefficients (FCCs) within glycolysis (Fig. 3A), gluconeogenesis
739 (Fig. 3B), and the TCA cycle (Fig. 3C) from the direct binding modular rate law [48], which is
740 equivalent to the reversible Michaelis-Menten kinetics [81] for simple reversible uni-uni
741 reactions, using theorems of Metabolic Control Analysis (MCA) [36,47]. In the direct binding
742 modular rate law, flux can be described by the effect of the maximal rate, the thermodynamics,
743 and the saturation of substrate [49]:

$$v = Ek_{\mathrm{cat}}^{+}\eta_{\mathrm{rev}}\eta_{\mathrm{sat,s}}, \tag{20}$$

$$\eta_{\mathrm{rev}} = 1 - \exp\left(\frac{\Delta_r G'}{RT}\right), \tag{21}$$

$$\eta_{\mathrm{sat,s}} = \frac{\prod_{i\in M^{\mathrm{s}}}\left(\frac{c_i}{K_{\mathrm{m},i}}\right)^{|S_i|}}{1 + \prod_{i\in M^{\mathrm{s}}}\left(\frac{c_i}{K_{\mathrm{m},i}}\right)^{|S_i|} + \prod_{i\in M^{\mathrm{p}}}\left(\frac{c_i}{K_{\mathrm{m},i}}\right)^{|S_i|}} \tag{22}$$

where M^{s} is substrates, M^{p} is products. From Eq. 20, we calculated the elasticity of substrate $\epsilon_{\mathrm{s},i}^{v}$ and product $\epsilon_{\mathrm{p},i}^{v}$:

$$\epsilon_{\mathrm{s},i}^{v} = \frac{\partial v}{\partial c_i}\frac{c_i}{v} = |S_i|\left(\eta_{\mathrm{rev}}^{-1} - \eta_{\mathrm{sat,s}}\right), \tag{23}$$

$$\epsilon_{\mathrm{p},i}^{v} = \frac{\partial v}{\partial c_i}\frac{c_{\mathrm{i}}}{v} = |S_i|\left(1 - \eta_{\mathrm{rev}}^{-1} - \eta_{\mathrm{sat,p}}\right), \tag{24}$$

$$\eta_{\mathrm{sat,p}} = \frac{\prod_{i\in M^{\mathrm{p}}}\left(\frac{c_i}{K_{\mathrm{m},i}}\right)^{|S_i|}}{1 + \prod_{i\in M^{\mathrm{s}}}\left(\frac{c_i}{K_{\mathrm{m},i}}\right)^{|S_i|} + \prod_{i\in M^{\mathrm{p}}}\left(\frac{c_i}{K_{\mathrm{m},i}}\right)^{|S_i|}}. \tag{25}$$

The stoichiometric matrices of the pathways we analyzed here are full rank, and each of their null spaces is one-dimensional, which means the degree of freedom of steady-state flux is one. For these pathways, the following Eq. 26 and 27 hold from the connectivity theorem and the summation theorem in MCA, respectively [50]:

$$\mathbf{C}_{\mathbf{v}}^{\mathbf{J}}\boldsymbol{\epsilon}_{\mathbf{c}}^{\mathbf{v}} = \mathbf{0}, \tag{26}$$

$$\sum_{j} C_{v_j}^{J} = 1, \tag{27}$$

$$\mathbf{C_v^J} = \begin{pmatrix} C_{v_1}^J & \cdots & C_{v_n}^J \\ \vdots & \ddots & \vdots \\ C_{v_1}^J & \cdots & C_{v_n}^J \end{pmatrix}, \tag{28}$$

$$\boldsymbol{\epsilon}_\mathbf{c}^\mathbf{v} = \begin{pmatrix} \epsilon_{c_1}^{v_1} & \cdots & \epsilon_{c_k}^{v_1} \\ \vdots & \ddots & \vdots \\ \epsilon_{c_1}^{v_n} & \cdots & \epsilon_{c_k}^{v_n} \end{pmatrix} \tag{29}$$

where $\epsilon_c^v = \{\epsilon_s^v, \epsilon_p^v\}$. Integrating Eq. 23, 24, 26, and 27, we obtained FCC as:

$$C_{v_l}^J = \frac{\alpha_l}{\sum_j \alpha_j}, \tag{30}$$

where α for GAPDH:PGK in glycolysis is described as

$$\alpha = \prod_{j=0}^{\text{ALDO}} \left(-\epsilon_\text{p}^{v_j}\right)\left(\epsilon_\text{s}^{v_\text{TPI}} - \epsilon_\text{p}^{v_\text{TPI}}\right) \prod_{j=l+1}^{n+1} \epsilon_\text{s}^{v_j}, \tag{31}$$

α for downstream reactions of GAPDH:PGK in glycolysis is described as

$$\alpha = \prod_{j=0}^{\text{ALDO}} \left(-\epsilon_\text{p}^{v_j}\right)\left(\epsilon_\text{s}^{v_\text{TPI}} - \epsilon_\text{p}^{v_\text{TPI}}\right) \prod_{j=\text{GAPDH:PGK}}^{l-1} \left(-\epsilon_\text{p}^{v_l}\right) \prod_{j=l+1}^{n+1} \epsilon_\text{s}^{v_j}, \tag{32}$$

α for ALDO in gluconeogenesis is described as

$$\alpha = \prod_{j=0}^{\text{GAPDH:PGK}} \left(-\epsilon_\text{p}^{v_j}\right)\left(\epsilon_\text{s}^{v_\text{TPI}} - \epsilon_\text{p}^{v_\text{TPI}}\right) \prod_{j=l+1}^{n+1} \epsilon_\text{s}^{v_j}, \tag{33}$$

α for downstream reactions of ALDO in gluconeogenesis is described as

$$\alpha = \prod_{j=0}^{\text{GAPDH:PGK}} \left(-\epsilon_\text{p}^{v_j}\right)\left(\epsilon_\text{s}^{v_\text{TPI}} - \epsilon_\text{p}^{v_\text{TPI}}\right) \prod_{j=\text{ALDO}}^{l-1} \left(-\epsilon_\text{p}^{v_j}\right) \prod_{j=l+1}^{n+1} \epsilon_\text{s}^{v_j}, \tag{34}$$

α for other reactions is described as

$$\alpha_l = \prod_{j=0}^{l-1}\left(-\epsilon_{\mathrm{p}}^{v_j}\right)\prod_{j=l+1}^{n+1}\epsilon_{\mathrm{s}}^{v_j}. \tag{35}$$

Note that reaction indices $j \in \{1, \ldots, N\}$ are denoted such that 1 represents the most upstream reaction and N represents the most downstream reaction in the pathway, and $\epsilon_{\mathrm{s}}^{v_0} = \epsilon_{\mathrm{p}}^{v_0} = \epsilon_{\mathrm{s}}^{v_{n+1}} = \epsilon_{\mathrm{p}}^{v_{n+1}} = 1$.

Metabolite concentrations and $\Delta_f G'^{\circ}$ values used in FCC calculation

We calculated FCCs under arbitrary $\Delta_r G'$ landscapes as well as under the hepatic ones. For both conditions, we used $\Delta_f G'^{\circ}$ values sampled for confidence interval calculation in GLEAM. To generate the hepatic $\Delta_r G'$ landscapes, we used metabolite concentrations sampled in the confidence interval calculation. To generate arbitrary $\Delta_r G'$ landscapes, logarithmic metabolite concentrations were uniformly sampled from the physiologically reasonable solution space $\Omega_{\ln c}$:

$$\Omega_{\ln c} = \left\{ \ln c \;\middle|\; \begin{array}{c} \Delta_r G_j' < 0 \\ lb_i \leq \ln c_i \leq ub_i \\ lb_i = ub_i = \ln c_i^{b*} \quad i \in M^{\mathrm{blood}} \end{array} \right\} \tag{36}$$

where M^{blood} represents blood metabolites. The upper and lower bounds of metabolite concentrations were the same as those used in GLEAM (Table S7). This sampling was performed 20 times for each $\Delta_f G'^{\circ}$ set using MATLAB function polySampler in the Volume-and-Sampling package [82]. Thus, we obtained 2000 × 20 = 40000 arbitrary $\Delta_r G'$ landscapes in total.

K_{m} values used in FCC calculation

In FCC calculation, we sampled Michaelis-Menten constants K_{m} for each $\Delta_r G'$ landscape to calculate reaction saturation level. To sample K_{m}, we first retrieved K_{m} and the turnover number, $k_{\mathrm{cat}} \in \{k_{\mathrm{cat}}^{+}, k_{\mathrm{cat}}^{-}\}$ values for enzymes of *Mus musculus*, *Rattus norvegicus*, *Homo sapiens*, *Bos taurus*, *Sus scrofa*, *Canis lupus familiaris*, and *Mammalia* [83] from BRENDA database [51]. For K_{m} and k_{cat} values from three or more data without reports of mutant enzymes, we calculated their logarithmic means and standard deviations. For K_{m} and k_{cat} from fewer than three data, we set the logarithmic mean of k_{cat} (/s) to 1 with a standard deviation of 1.5, and the logarithmic mean of K_{m} (mM) to −1 with a standard deviation of 1 [84]. With the means and standard deviations of K_{m} and k_{cat}, we uniformly sampled logarithmic K_{m}, k_{cat} values for each enzyme from the solution space Ω_{KP}:

$$\Omega_{\mathrm{KP},j} = \left\{ \begin{pmatrix} \log K_{\mathrm{m}} \\ \log k_{\mathrm{cat}} \end{pmatrix} \middle| \begin{array}{c} \log \mu^{K_{\mathrm{m},i,j}} - 2\sigma^{K_{\mathrm{m},i,j}} \leq \log K_{\mathrm{m},i,j} \leq \log \mu^{K_{\mathrm{m},i,j}} + 2\sigma^{K_{\mathrm{m},i,j}} \\ \log \mu^{k_{\mathrm{cat},j}} - 2\sigma^{k_{\mathrm{cat},j}} \leq \log k_{\mathrm{cat},j} \leq \log \mu^{k_{\mathrm{cat},j}} + 2\sigma^{k_{\mathrm{cat},j}} \\ \log k_{\mathrm{cat},j}^{+} - \log k_{\mathrm{cat},j}^{-} - \sum_{i \in M^{\mathrm{s}}} \log K_{\mathrm{m},i,j}^{|S_{i,j}|} + \sum_{i \in M^{\mathrm{p}}} \log K_{\mathrm{m},i,j}^{|S_{i,j}|} = \log K_{\mathrm{eq},j} \\ K_{\mathrm{eq},j} = \exp\left(-\frac{1}{RT} \sum_{i \in M} S_{i,j} \Delta_f G_i'^{\circ} \right) \end{array} \right\}, \quad (37)$$

$\forall i \in M, \forall j \in N$

where μ is mean, σ is standard deviation, and K_{eq} is equilibrium constant. The third constraint reflects the Haldane relationship [81]. These samplings were performed 20 times for each $\Delta_r G'$ landscape using MATLAB function polySampler in the Volume-and-Sampling

787 package [82]. Thus, we finally calculated FCC under the arbitrary and hepatic $\Delta_r G'$
788 landscapes with 20 × 20 × 2000 = 800000 and 20 × 2000 = 40000 sets of metabolite
789 concentrations, $\Delta_f G'^{\circ}$ and K_{m} values, respectively.
790

791 **Definitions of EC and total EC**

792 By solving the equation of the direct binding modular rate law (Eq. 20) with respect to
793 enzyme amount, we can obtain enzyme demand needed to carry a certain flux:

$$E = \frac{v}{k_{\mathrm{cat}}^{+}} \eta_{\mathrm{rev}}^{-1} \eta_{\mathrm{sat,s}}^{-1}. \tag{38}$$

794 With this equation, we defined Enzyme Cost (EC) as the product of the enzyme demand and
795 the enzyme molecular weight *w*:

$$\mathrm{EC} = wE. \tag{39}$$

796 The enzyme molecular weights were retrieved from the UniProt database [85]. We also defined
797 pathway's total EC as the sum of ECs in the pathway:

$$\text{total EC} = \sum_{j \in N^{\mathrm{pathway}}} \mathrm{EC}_j \tag{40}$$

798 where N^{pathway} is reactions included in the pathway. We calculated ECs in glycolysis (Fig.
799 3A), gluconeogenesis (Fig. 3B), and the TCA cycle (Fig. 3C), which were the same as those
800 used in FCC calculations, under the hepatic $\Delta_r G'$ landscape using metabolite concentrations
801 and $\Delta_f G'^{\circ}$ values sampled for confidence interval calculation in GLEAM, and geometric
802 mean of K_{m} values from the BRENDA database [51] obtained in FCC calculation (Table S5).
803 For K_{m} with fewer than three data found in the BRENDA, we set their c/K_{m} values to the

geometric mean of the pathway. k_{cat}^{+} values were assumed to be the same within a pathway, and their effect can be ignored in this study because we only focused on the relative values of EC.

Minimization of total EC

Since EC is dependent on metabolite concentrations, we defined Enzyme Cost Minimum (ECM) as a theoretical condition where total EC is minimized with metabolite concentrations. We obtained ECM by solving the following non-linear optimization problem [42]:

$$
\begin{aligned}
\min_{\ln c} \quad & \text{total EC} = \sum_{j \in N^{\mathrm{pathway}}} \mathrm{EC}_j \\
\text{s.t.} \quad & \mathrm{EC}_j = wv\eta_{\mathrm{rev},j}^{-1}\eta_{\mathrm{sat,s},j}^{-1}, \ \ j \in N \\
& \eta_{\mathrm{rev},j} = 1 - \exp\left(\frac{\Delta_r G_j'}{RT}\right) \\
& \eta_{\mathrm{sat,s},j} = \frac{\prod_{i \in M^{\mathrm{s}}} \left(\frac{c_i}{K_{\mathrm{m},i,j}}\right)^{|S_{i,j}|}}{1 + \prod_{i \in M^{\mathrm{s}}} \left(\frac{c_i}{K_{\mathrm{m},i,j}}\right)^{|S_{i,j}|} + \prod_{i \in M^{\mathrm{p}}} \left(\frac{c_i}{K_{\mathrm{m},i,j}}\right)^{|S_{i,j}|}} \\
& \Delta_r G_j' = \sum_{i \in M} S_{i,j}\left(\Delta_f G_i'^{\circ,\mathrm{liver}} + RT \ln c_i\right) < 0, \ \ j \in N \\
& lb_i \le \ln c_i \le ub_i, \ \ i \in M \\
& lb_i = ub_i = \ln c_i^{\mathrm{mouse}}, \ \ i \in M^{\mathrm{blood}} \\
& lb_i = ub_i = \ln c_i^{\mathrm{mouse}}, \ \ i \in M^{\mathrm{terminal}} \\
& \ln \frac{c_{i_1}}{c_{i_2}} = \left(\ln \frac{c_{i_1}}{c_{i_2}}\right)^{\mathrm{mouse}}, \ \ \forall (i_1, i_2) \in M^{\mathrm{cofactor}}.
\end{aligned}
\tag{41}
$$

812 *w* and *v* are normalized by the minimum molecular weight and flux, respectively. The relative
813 flux values for a pathway we analyzed were unique because the degree of freedom of these
814 pathways' steady flux is 1. $\ln c^{\mathrm{mouse}}$ represents metabolite concentration in mouse *i.e.*,
815 $\ln c^{*}$ and $\ln c^{b*}$. M^{blood} represents blood metabolites, and M^{terminal} represents
816 intracellular metabolites at the termini of each pathway: Glucose and Pyr for glycolysis and
817 gluconeogenesis, and AcCoA, OAA, and Mal for the TCA cycle. By fixing these
818 concentrations and cofactor ratios to those in mouse liver, the total Gibbs free energy change
819 across the entire pathway in ECM is consistent with that in the mouse liver. ECM was
820 calculated by MATLAB function fmincon with termination tolerance on the first-order
821 optimality of OptimalityTolerance = 10^{-7}, tolerance on the constraint violation of
822 ConstraintTolerance = 10^{-9}, maximum number of function evaluations of
823 MaxFunctionEvaluations = 1000000, and maximum number of iterations of MaxIterations =
824 100000. The optimization was performed 100 times for a single problem, and the solution
825 minimizing the objective function was selected as ECM.
826
827 **Calculation of MEG**
828 To quantify the efficiency of metabolic switching in terms of metabolite concentration
829 changes, we defined the Metabolite Equilibrium Gap (MEG) as the minimum concentration
830 changes required to reverse the direction of metabolism:

$$\begin{aligned} &\mathrm{MEG} = \exp A \\ &A = \min_{\ln c} \sqrt{\frac{1}{\#M}\sum_{i\in M}\left(\ln c_i - \ln c_i^{\mathrm{sys}}\right)^2} \\ \text{s.t.}\quad &\Delta_r G_j' = \sum_{i\in M} S_{i,j}\left(\Delta_f G_i'^{\circ} + RT\ln c_i\right) = 0, \quad j \in N^{\mathrm{shift}} \\ &\Delta_r G_j' = \sum_{i\in M} S_{i,j}\left(\Delta_f G_i'^{\circ} + RT\ln c_i\right) < 0, \quad j \in N \notin N^{\mathrm{shift}} \\ &b_i \le \ln c_i \le ub_i, \ \ j \in M \end{aligned} \tag{42}$$

where sys represents a value in a target system corresponding to the liver or ECM in this study. N^{shift} is the reactions that must proceed in the reverse direction when switching metabolisms; it includes reversible reactions in glycolysis and gluconeogenesis, and all reactions in the TCA cycle. $\Delta_f G'^{\circ}$ values used in MEG calculation were the same as those in the liver (and also the same as those in ECM). MEG was calculated using Gurobi [72] MATLAB API with dual feasibility tolerance of OptimalityTol = 10^{-9} and primal feasibility tolerance of FeasibilityTol = 10^{-9}.

QUANTIFICATION AND STATISTICAL ANALYSIS

Statistical tests, optimizations, computational samplings, and calculations of $\Delta_r G'$, FCC, and EC were performed using MATLAB 2021b (The MathWorks Inc.) and Gurobi (version 10.0.3) [72]. Database handlings were performed using Python (version 3.10. All details of statistical tests are described in the Results section. The MATLAB package Plot Groups of Stacked Bars [86] was used to create the figures.

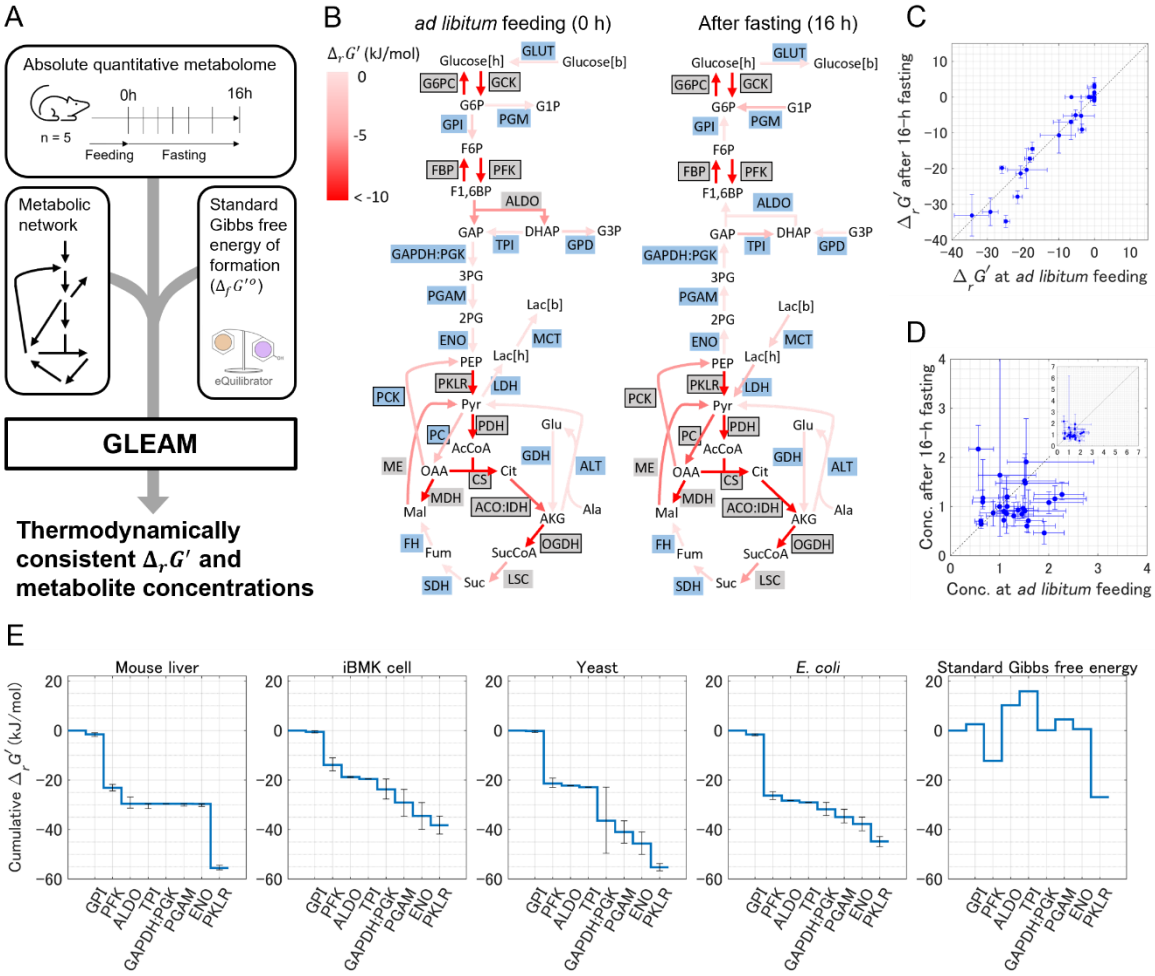

Fig. 1: $\Delta_r G'$ landscape is robust against fasting despite metabolite concentration fluctuations

(**A**) Overview of the application of GLEAM to estimate $\Delta_r G'$ landscape in the mouse liver. Metabolomic data were acquired from the liver, skeletal muscle, and plasma of WT and *ob*/*ob* mice during fasting (Table S1) [8,66]. n = 5 biological replicates were used per group. The estimated metabolite concentrations, $\Delta_f G'^{\circ}$, and $\Delta_r G'$ values by GLEAM are shown in Table S2. (**B**) $\Delta_r G'$ landscape of glucose metabolism in mouse liver at *ad libitum* feeding and after 16-hour fasting. $\Delta_r G'$ is depicted by arrow colors. Shaded texts represent reaction

855 names; boxed reactions are irreversible, while unboxed reactions are reversible. Blue
856 shadings indicate near-equilibrium reactions with $\Delta_r G' > -5$ kJ/mol, and gray shadings
857 indicate the other reactions with $\Delta_r G' \leq -5$ kJ/mol. Unshaded texts represent metabolites.
858 [h], [m], and [b] indicate hepatic, myocytic, and blood metabolites, respectively.
859 Abbreviations of reactions and metabolites are defined in the glossary and Table S3. (**C**)
860 Comparison of $\Delta_r G'$ in WT mouse liver at *ad libitum* feeding and after 16-hour fasting. The
861 forward direction ($\Delta_r G' < 0$) is defined as the reaction direction at *ad libitum* feeding. Error
862 bars show 95% confidence intervals. (**D**) Comparison of metabolite concentrations in WT
863 mouse liver at *ad libitum* feeding and after 16-hour fasting. Plotted metabolite concentrations
864 represent those normalized by the mean value at all seven time points and two genotypes (14
865 conditions in total) to eliminate scale differences in concentrations among metabolites. Error
866 bars show 95% confidence intervals. (**E**) Comparison of $\Delta_r G'$ in glycolysis across cell types
867 and organisms. The data in iBMK cell, yeast, and *E. coli* were measured using LC-MS and
868 isotope tracers [26]. Standard Gibbs free energy was calculated by treating all metabolite
869 concentrations as 1 M. The vertical axis represents cumulative $\Delta_r G'$ from GPI. Error bars
870 show 95% confidence intervals.
871
872

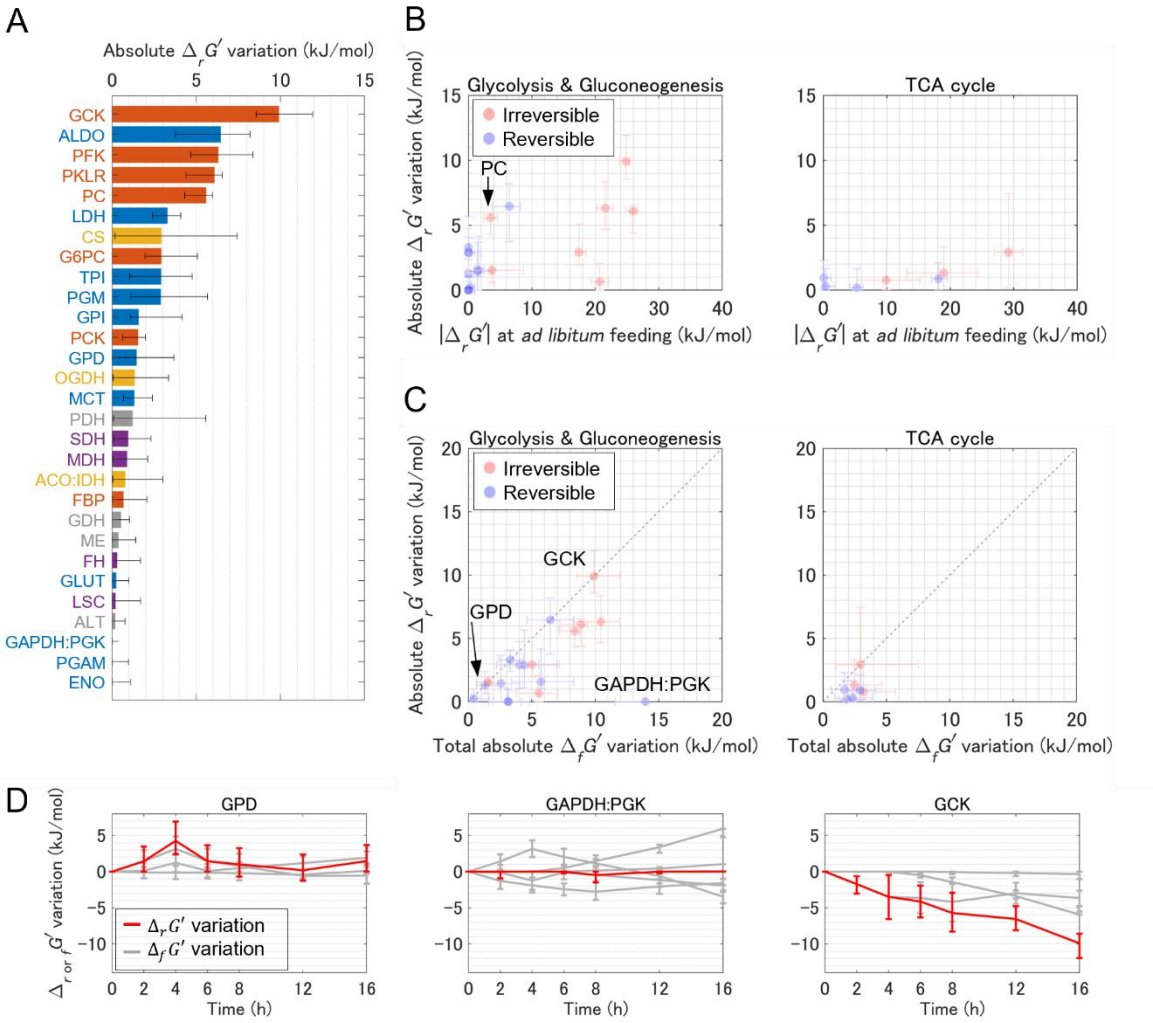

873

874 **Fig. 2: $\Delta_r G'$ maintenance during fasting is associated with metabolite concentration**

875 **fluctuations in different ways among pathways**

876 (**A**) Absolute $\Delta_r G'$ variation = $|\Delta_r G'_{16\mathrm{h}} - \Delta_r G'_{0\mathrm{h}}|$. Bars depict irreversible reactions in

877 glycolysis and gluconeogenesis (orange), reversible reactions in glycolysis and

878 gluconeogenesis (blue), irreversible reactions in the TCA cycle (yellow), reversible reactions

879 in the TCA cycle (purple), and the other reactions in the metabolic network (grey),

880 respectively. Error bars show 95% confidence intervals. (**B**) Relationship between absolute

881 $\Delta_r G'$ variation and reaction distance from equilibrium represented by absolute $\Delta_r G'$ at *ad*
882 *libitum* feeding. Error bars show 95% confidence intervals. The reaction PC is highlighted
883 and discussed in the Results section. (**C**) Comparison of absolute $\Delta_r G'$ variation of reactions
884 and total absolute $\Delta_f G'$ variation of metabolites. Absolute $\Delta_f G'$ variation is dependent on
885 concentrations of metabolites involved in the reaction, and defined by $\sum\left|S\left(\Delta_f G'_{16h} -\right.\right.$
886 $\left.\left.\Delta_f G'_{0h}\right)\right|$. When $\Delta_f G'$ variation = $S\left(\Delta_f G'_{16h} - \Delta_f G'_{0h}\right)$ of the metabolites involved in the
887 reaction are cancelled out, absolute $\Delta_r G'$ variation is smaller than total absolute $\Delta_f G'$
888 variation, resulting in the reaction being plotted in the lower right. Plotted reactions for
889 glycolysis and gluconeogenesis, and the TCA cycles are the same as Fig. 2B. Error bars show
890 95% confidence intervals. The reactions GPD, GAPDH:PGK and GCK are highlighted and
891 discussed in the Results section. (**D**) Time courses of $\Delta_r G'$ variation and $\Delta_f G'$ variation
892 for representative reactions: GPD (small $\Delta_f G'$ variations), GAPDH:PGK (large $\Delta_f G'$
893 variations which are canceled out), and GCK (large $\Delta_f G'$ variations which are not canceled
894 out). Red and grey lines depict $\Delta_r G'$ variation and $\Delta_f G'$ variation, respectively. Error bars
895 show 95% confidence intervals.
896

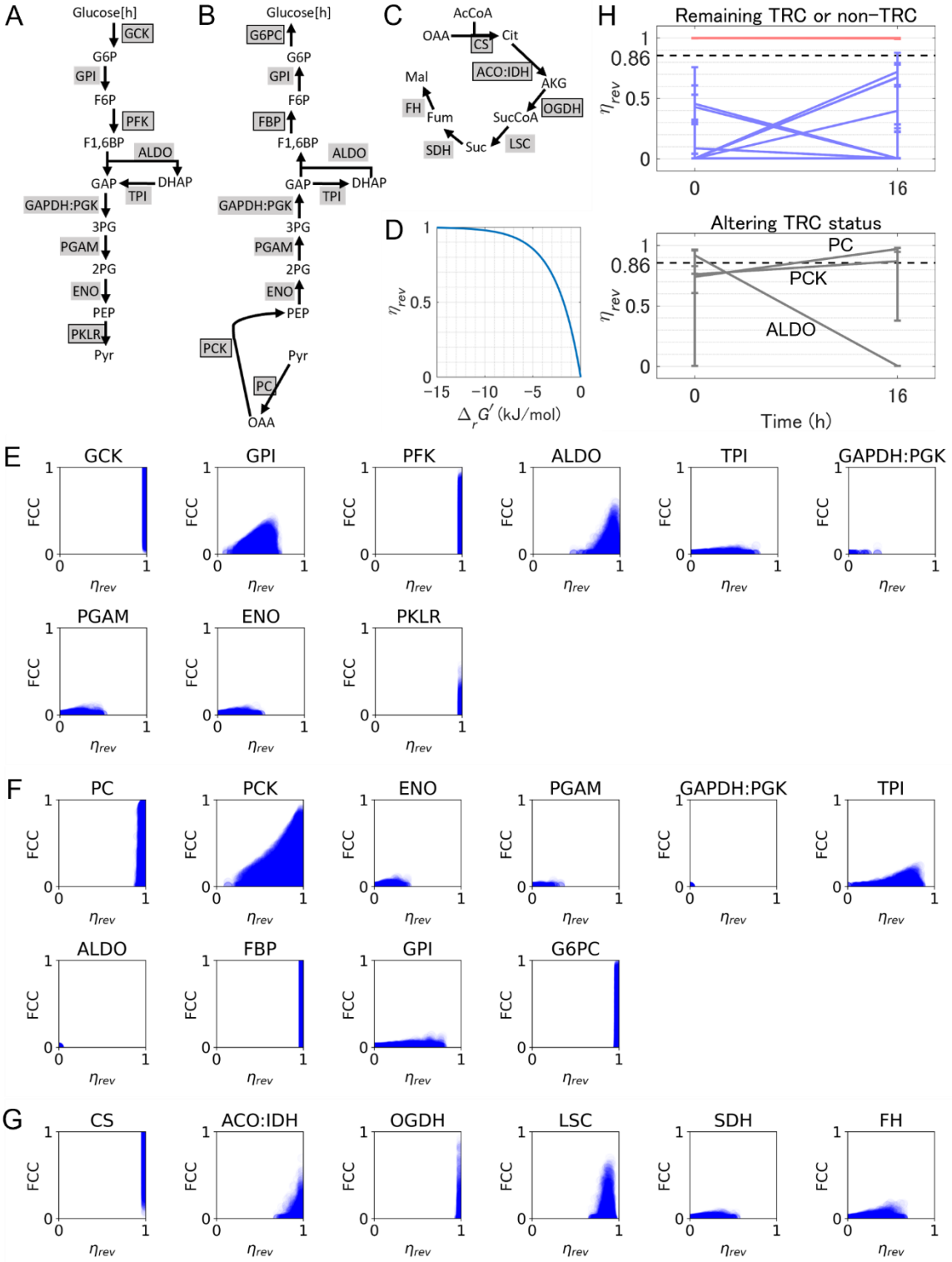
A
Glucose[h]
GCK
G6P
GPI
F6P
PFK
F1,6BP
ALDO
GAP
DHAP
TPI
GAPDH:PGK
3PG
PGAM
2PG
ENO
PEP
PKLR
Pyr
B
Glucose[h]
G6PC
G6P
GPI
F6P
FBP
F1,6BP
ALDO
GAP
DHAP
TPI
GAPDH:PGK
3PG
PGAM
2PG
ENO
PEP
PCK
Pyr
PC
OAA
C
AcCoA
OAA
CS
Cit
ACO:IDH
AKG
OGDH
SucCoA
LSC
Suc
SDH
Fum
FH
Mal
D
η_{rev}
$\Delta_r G'$ (kJ/mol)
H
Remaining TRC or non-TRC
Altering TRC status
PC
PCK
ALDO
Time (h)
E
GCK
GPI
PFK
ALDO
TPI
GAPDH:PGK
PGAM
ENO
PKLR
F
PC
PCK
ENO
PGAM
GAPDH:PGK
TPI
ALDO
FBP
GPI
G6PC
G
CS
ACO:IDH
OGDH
LSC
SDH
FH
FCC
η_{rev}

897

898 **Fig. 3: Thermodynamic Rate-limiting Candidates (TRCs) were maintained during**
899 **fasting**

900 (**A**) Glycolysis pathway where FCCs were calculated. (**B**) Gluconeogenesis pathway where
901 FCCs were calculated. (**C**) The TCA cycle where FCCs were calculated. MDH was excluded
902 from this TCA cycle because it proceeded in the opposite direction to the oxidative TCA
903 cycle. (**D**) Correspondence between $\Delta_r G'$ and η_{rev}. (**E-G**) Relationship between η_{rev} and
904 FCC in glycolysis (**E**), gluconeogenesis (**F**), and the TCA cycle (**G**) in the mouse liver. η_{rev}
905 and FCC values of each point were calculated from each sampled set of metabolite
906 concentrations and $\Delta_f G'^{\circ}$ values for the calculation of confidence intervals and sampled
907 K_{m} values based on BRENDA database (see Methods). Metabolite concentrations at *ad*
908 *libitum* feeding were used for glycolysis (**E**) and the TCA cycle (**G**), and those after 16-hour
909 fasting were used for gluconeogenesis (**F**). Vertical variation is attributed to differences in
910 K_{m} values and condition of the other reactions, while horizontal variation reflects differences
911 in metabolite concentrations and $\Delta_f G'^{\circ}$. (**H**) Alterations of TRC status based on transitions
912 in η_{rev} for reactions in glycolysis and gluconeogenesis before and after starvation. Red, blue,
913 and grey lines depict reactions remaining TRC (5 reactions), reactions remaining non-TRC
914 (10 reactions), and reactions altering their TRC status (either TRC or not) during fasting (3
915 reactions), respectively. Black dashed lines indicate the boundary between TRC and non-
916 TRC where $\eta_{rev} = 0.86$ *i.e.*, $\Delta_r G' = -5\ \mathrm{kJ/mol}$. Error bars show 95% confidence
917 intervals.

918

919

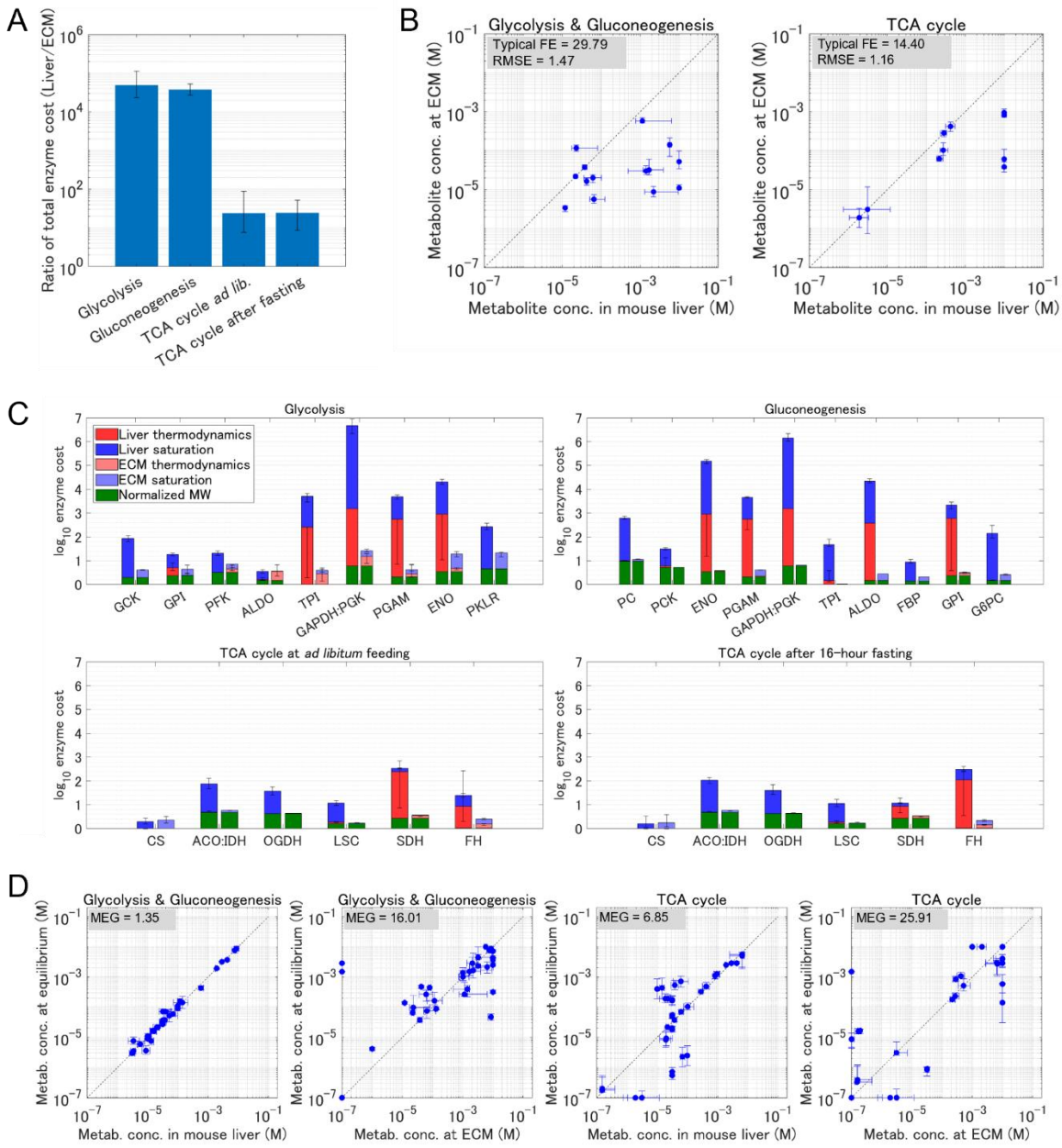

Fig. 4: Glycolysis and gluconeogenesis achieve efficient switching by expending large Enzyme Costs

923 (**A**) Ratio of total enzyme cost under metabolite concentrations in the mouse liver and ECM
924 (Liver/ECM). The total EC was calculated for glycolysis, gluconeogenesis, and the TCA
925 cycle, which are the same as the pathways used for FCC calculation (Fig. 3A to C).
926 Metabolite concentrations at *ad libitum* feeding and after 16-hour fasting were used for
927 glycolysis and gluconeogenesis, respectively. K_{m} values for EC calculation were the
928 geometric mean of data in the BRENDA database (Table S5). Error bars show 95%
929 confidence intervals. EC in mouse liver, and metabolite concentrations and EC at ECM are
930 shown in Table S5. (**B**) Comparison of metabolite concentrations in the mouse liver and ECM.
931 Plotted data are for the measured metabolites, and the scatter plot for the TCA cycle includes
932 the data both at *ad libitum* feeding and after 16-hour fasting. RMSE is the root mean square
933 error on a $\log_{10}$-scale of ECM's prediction compared to metabolite concentrations in the
934 mouse liver, and typical fold error (typical FE) = 10^{RMSE}. Error bars show 95% confidence
935 intervals. Plotted data are for the measured metabolites. (**C**) EC of each reaction in glycolysis,
936 gluconeogenesis, and the TCA cycle. The left and right bars of each reaction are EC in the
937 mouse liver and ECM, respectively. Since the vertical axis represents a logarithmic scale, EC
938 can be depicted by the stacked bar of normalized enzyme molecular weight (green), the effect
939 of thermodynamics, η_{rev}^{-1} (red), and saturation, $\eta_{\mathrm{sat,s}}^{-1}$ (blue). Note that although the total
940 Gibbs free energy change across the entire pathway in ECM is fixed to that in the mouse liver
941 (see Methods), the sum of η_{rev}^{-1} differs due to the non-linear increase of η_{rev} over $\Delta_r G'$
942 (Fig. 3D). Error bars show 95% confidence intervals. (**D**) Comparison of metabolite
943 concentrations in the liver or ECM, and those for MEG calculation, where the reactions
944 required to reverse for metabolic switching are at equilibrium. Plotted data are for the

measured metabolites. Error bars show 95% confidence intervals. Metabolite concentrations where the reactions required to reverse for metabolic switching are at equilibrium are shown in Table S6.

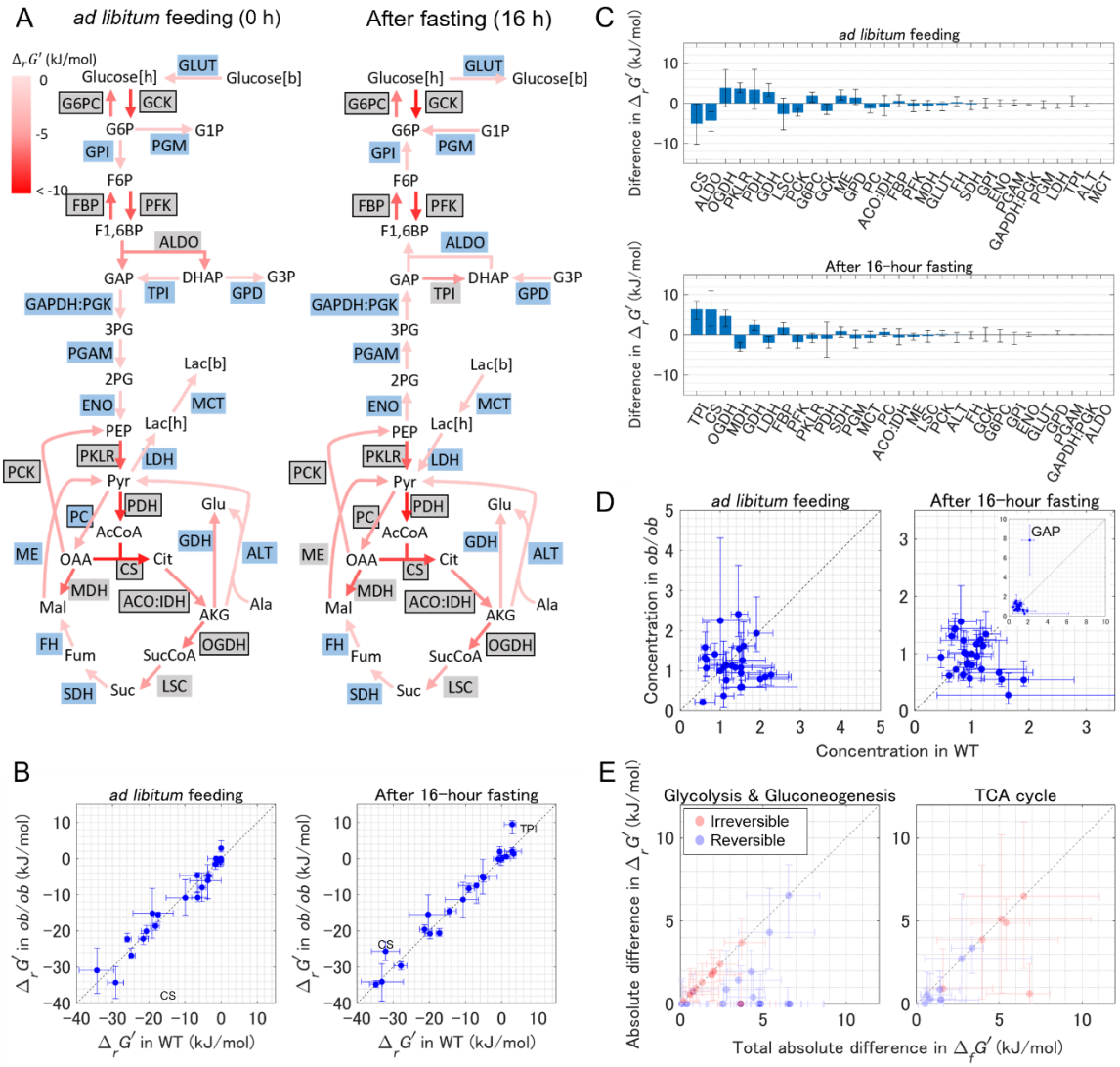

Fig. 5: Robustness of $\Delta_r G'$ in the liver against obesity

(**A**) $\Delta_r G'$ landscape of glucose metabolism in *ob*/*ob* mouse liver at *ad libitum* feeding and after 16-hour fasting. $\Delta_r G'$ is depicted by arrow colors. Shaded texts represent reaction names; boxed reactions are irreversible, while unboxed reactions are reversible. Blue shadings indicate near-equilibrium reactions with $\Delta_r G' > -5$ kJ/mol, and gray shadings indicate the other reactions with $\Delta_r G' \leq -5$ kJ/mol. Unshaded texts represent metabolites.

The estimated metabolite concentrations, $\Delta_f G'^{\circ}$, and $\Delta_r G'$ values by GLEAM are shown in Table S2. (**B**) Comparison of $\Delta_r G'$ in WT and *ob*/*ob* mouse liver. The forward direction ($\Delta_r G' < 0$) is defined as the reaction direction in WT at *ad libitum* feeding. Error bars show 95% confidence intervals. (**C**) Difference in $\Delta_r G'$ between WT and *ob*/*ob* mouse liver ($\Delta_r G'_{ob/ob} - \Delta_r G'_{\mathrm{WT}}$). Reactions are arranged from left to right in order of decreasing absolute difference in $\Delta_r G'$. Error bars show 95% confidence intervals. (**D**) Comparison of metabolite concentrations in WT and *ob*/*ob* mouse liver. Plotted data represent the concentrations normalized by the mean value at all seven time points and two genotypes *(i.e.*, 14 conditions) to eliminate scale differences in concentrations among metabolites. Error bars show 95% confidence intervals. (**E**) Comparison of absolute difference in $\Delta_r G'$ variation and total absolute deference in $\Delta_f G' = \sum \left| S\left(\Delta_f G'_{ob/ob} - \Delta_f G'_{\mathrm{WT}}\right) \right|$, between WT and *ob*/*ob* mouse liver. Plotted data includes those at *ad libitum* feeding and after 16-hour fasting. The reactions for glycolysis and gluconeogenesis, and the TCA cycles are the same as Fig. 2B. Error bars show 95% confidence intervals.

REFERENCES

1. Scrutton, M.C., and Utter, M.F. (1968). The Regulation of Glycolysis and Gluconeogenesis in Animal Tissues. Annu. Rev. Biochem. *37*, 249–302.

2. Rothman, D.L., Magnusson, I., Katz, L.D., Shulman, R.G., and Shulman, G.I. (1991). Quantitation of Hepatic Glycogenolysis And Gluconeogenesis in Fasting Humans With ^{13}C NMR. Science *254*, 573–576.

3. Nordlie, R.C., Foster, J.D., and Lange, A.J. (1999). Regulation of glucose production by the liver. Annu. Rev. Nutr. *19*, 379–406.

4. Moore, M.C., Coate, K.C., Winnick, J.J., An, Z., and Cherrington, A.D. (2012). Regulation of hepatic glucose uptake and storage in vivo. Adv. Nutr. *3*, 286–294.

5. Han, H.-S., Kang, G., Kim, J.S., Choi, B.H., and Koo, S.-H. (2016). Regulation of glucose metabolism from a liver-centric perspective. Exp. Mol. Med. *48*, e218.

6. Katz, J., and Tayek, J.A. (1998). Gluconeogenesis and the Cori cycle in 12-, 20-, and 40-h-fasted humans. American Journal of Physiology-Endocrinology and Metabolism *275*, E537–E542.

7. Egami, R., Kokaji, T., Hatano, A., Yugi, K., Eto, M., Morita, K., Ohno, S., Fujii, M., Hironaka, K.-I., Uematsu, S., et al. (2021). Trans-omic analysis reveals obesity-associated dysregulation of inter-organ metabolic cycles between the liver and skeletal muscle. iScience *24*, 102217.

8. Morita, K., Hatano, A., Kokaji, T., Sugimoto, H., Tsuchiya, T., Ozaki, H., Egami, R., Li, D., Terakawa, A., Ohno, S., et al. (2025). Structural robustness and temporal vulnerability of the starvation-responsive metabolic network in healthy and obese mouse liver. Sci. Signal. *18*, eads2547.

9. Samuel, V.T., and Shulman, G.I. (2016). The pathogenesis of insulin resistance: integrating signaling pathways and substrate flux. J. Clin. Invest. *126*, 12–22.

10. Stern, J.H., Smith, G.I., Chen, S., Unger, R.H., Klein, S., and Scherer, P.E. (2019). Obesity dysregulates fasting-induced changes in glucagon secretion. J. Endocrinol. *243*, 149–160.

11. Stocks, B., Gonzalez-Franquesa, A., Borg, M.L., Björnholm, M., Niu, L., Zierath, J.R., and Deshmukh, A.S. (2022). Integrated Liver and Plasma Proteomics in Obese Mice Reveals Complex Metabolic Regulation. Mol. Cell. Proteomics *21*, 100207.

12. Bai, Y., Morita, K., Kokaji, T., Hatano, A., Ohno, S., Egami, R., Pan, Y., Li, D., Yugi, K., Uematsu, S., et al. (2024). Trans-omic analysis reveals opposite metabolic dysregulation between feeding and fasting in liver associated with obesity. iScience *27*, 109121.

1005 13. Magnusson, I., Rothman, D.L., Katz, L.D., Shulman, R.G., and Shulman, G.I. (1992).
1006 Increased rate of gluconeogenesis in type II diabetes mellitus. A 13C nuclear magnetic
1007 resonance study. J. Clin. Invest. *90*, 1323–1327.

1008 14. Hundal, R.S., Krssak, M., Dufour, S., Laurent, D., Lebon, V., Chandramouli, V., Inzucchi,
1009 S.E., Schumann, W.C., Petersen, K.F., Landau, B.R., et al. (2000). Mechanism by which
1010 metformin reduces glucose production in type 2 diabetes. Diabetes *49*, 2063–2069.

1011 15. Wajngot, A., Chandramouli, V., Schumann, W.C., Ekberg, K., Jones, P.K., Efendic, S.,
1012 and Landau, B.R. (2001). Quantitative contributions of gluconeogenesis to glucose
1013 production during fasting in type 2 diabetes mellitus. Metabolism *50*, 47–52.

1014 16. Petersen, K.F., Price, T.B., and Bergeron, R. (2004). Regulation of Net Hepatic
1015 Glycogenolysis and Gluconeogenesis during Exercise: Impact of Type 1 Diabetes. J.
1016 Clin. Endocrinol. Metab. *89*, 4656–4664.

1017 17. Petersen, M.C., Vatner, D.F., and Shulman, G.I. (2017). Regulation of hepatic glucose
1018 metabolism in health and disease. Nat. Rev. Endocrinol. *13*, 572–587.

1019 18. Schramm, T.K., Gislason, G.H., Køber, L., Rasmussen, S., Rasmussen, J.N., Abildstrøm,
1020 S.Z., Hansen, M.L., Folke, F., Buch, P., Madsen, M., et al. (2008). Diabetes Patients
1021 Requiring Glucose-Lowering Therapy and Nondiabetics With a Prior Myocardial
1022 Infarction Carry the Same Cardiovascular Risk. Circulation *117*, 1945–1954.

1023 19. Spencer, E.A., Pirie, K.L., Stevens, R.J., Beral, V., Brown, A., Liu, B., Green, J., and
1024 Reeves, G.K. (2008). Diabetes and modifiable risk factors for cardiovascular disease:
1025 the prospective Million Women Study. Eur. J. Epidemiol. *23*, 793–799.

1026 20. Gancheva, S., Jelenik, T., Álvarez-Hernández, E., and Roden, M. (2018). Interorgan
1027 metabolic crosstalk in human insulin resistance. Physiol. Rev. *98*, 1371–1415.

1028 21. Annesley, T.M. (2003). Ion suppression in mass spectrometry. Clin. Chem. *49*, 1041–
1029 1044.

1030 22. Mashego, M.R., Wu, L., Van Dam, J.C., Ras, C., Vinke, J.L., Van Winden, W.A., Van
1031 Gulik, W.M., and Heijnen, J.J. (2004). MIRACLE: mass isotopomer ratio analysis of U-
1032 13C-labeled extracts. A new method for accurate quantification of changes in
1033 concentrations of intracellular metabolites. Biotechnol. Bioeng. *85*, 620–628.

1034 23. Sugimoto, M., Hirayama, A., Robert, M., Abe, S., Soga, T., and Tomita, M. (2010).
1035 Prediction of metabolite identity from accurate mass, migration time prediction and
1036 isotopic pattern information in CE-TOFMS data. Electrophoresis *31*, 2311–2318.

1037 24. Bennett, B.D., Kimball, E.H., Gao, M., Osterhout, R., Van Dien, S.J., and Rabinowitz,
1038 J.D. (2009). Absolute metabolite concentrations and implied enzyme active site
1039 occupancy in Escherichia coli. Nat. Chem. Biol. *5*, 593–599.

1040 25. Canelas, A.B., Ras, C., ten Pierick, A., van Gulik, W.M., and Heijnen, J.J. (2011). An in
1041 vivo data-driven framework for classification and quantification of enzyme kinetics and
1042 determination of apparent thermodynamic data. Metab. Eng. *13*, 294–306.

1043 26. Park, J.O., Rubin, S.A., Xu, Y.F., Amador-Noguez, D., Fan, J., Shlomi, T., and
1044 Rabinowitz, J.D. (2016). Metabolite concentrations, fluxes and free energies imply
1045 efficient enzyme usage. Nat. Chem. Biol. *12*, 482–489.

1046 27. Niebel, B., Leupold, S., and Heinemann, M. (2019). An upper limit on Gibbs energy
1047 dissipation governs cellular metabolism. Nature Metabolism *1*, 125–132.

1048 28. Mavrovouniotis, M.L. (1993). Identification of localized and distributed bottlenecks in
1049 metabolic pathways. Proc. Int. Conf. Intell. Syst. Mol. Biol. *1*, 275–283.

1050 29. Henry, C.S., Jankowski, M.D., Broadbelt, L.J., and Hatzimanikatis, V. (2006). Genome-
1051 Scale Thermodynamic Analysis of Escherichia coli Metabolism. Biophys. J. *90*, 1453–
1052 1461.

1053 30. Feist, A.M., Henry, C.S., Reed, J.L., Krummenacker, M., Joyce, A.R., Karp, P.D.,
1054 Broadbelt, L.J., Hatzimanikatis, V., and Palsson, B.Ø. (2007). A genome-scale metabolic
1055 reconstruction for Escherichia coli K-12 MG1655 that accounts for 1260 ORFs and
1056 thermodynamic information. Mol. Syst. Biol. *3*, 121.

1057 31. Henry, C.S., Broadbelt, L.J., and Hatzimanikatis, V. (2007). Thermodynamics-based
1058 metabolic flux analysis. Biophys. J. *92*, 1792–1805.

1059 32. Soh, K.C., and Hatzimanikatis, V. (2010). Network thermodynamics in the post-genomic
1060 era. Curr. Opin. Microbiol. *13*, 350–357.

1061 33. Hamilton, J.J., Dwivedi, V., and Reed, J.L. (2013). Quantitative assessment of
1062 thermodynamic constraints on the solution space of genome-scale metabolic models.
1063 Biophys. J. *105*, 512–522.

1064 34. Seep, L., Razaghi-Moghadam, Z., and Nikoloski, Z. (2021). Reaction lumping in
1065 metabolic networks for application with thermodynamic metabolic flux analysis. Sci.
1066 Rep. *11*, 8544.

1067 35. Janasch, M., Crang, N., Asplund-Samuelsson, J., Sporre, E., Bruch, M., Gynnå, A., Jahn,
1068 M., and Hudson, E.P. (2022). Thermodynamic limitations of PHB production from
1069 formate and fructose in Cupriavidus necator. Metab. Eng. *73*, 256–269.

1070 36. Kacser, H., and Burns, J.A. (1973). The control of flux. Symp. Soc. Exp. Biol. *27*, 65–
1071 104.

1072 37. Dai, Z., and Locasale, J.W. (2018). Thermodynamic constraints on the regulation of
1073 metabolic fluxes. J. Biol. Chem. *293*, 19725–19739.

38. van Niekerk, D.D., Rust, E., Bruggeman, F., Westerhoff, H.V., and Snoep, J.L. (2023). Is distance from equilibrium a good indicator for a reaction's flux control? Biosystems. *232*, 104988.

39. Flamholz, A., Noor, E., Bar-Even, A., Liebermeister, W., and Milo, R. (2013). Glycolytic strategy as a tradeoff between energy yield and protein cost. Proceedings of the National Academy of Sciences *110*, 10039–10044.

40. Tepper, N., Noor, E., Amador-Noguez, D., Haraldsdóttir, H.S., Milo, R., Rabinowitz, J., Liebermeister, W., and Shlomi, T. (2013). Steady-State Metabolite Concentrations Reflect a Balance between Maximizing Enzyme Efficiency and Minimizing Total Metabolite Load. PLoS One *8*, e75370.

41. Noor, E., Bar-Even, A., Flamholz, A., Reznik, E., Liebermeister, W., and Milo, R. (2014). Pathway Thermodynamics Highlights Kinetic Obstacles in Central Metabolism. PLoS Comput. Biol. *10*. https://doi.org/10.1371/journal.pcbi.1003483.

42. Noor, E., Flamholz, A., Bar-Even, A., Davidi, D., Milo, R., and Liebermeister, W. (2016). The Protein Cost of Metabolic Fluxes: Prediction from Enzymatic Rate Laws and Cost Minimization. PLoS Comput. Biol. *12*, e1005167.

43. Soga, T., Ohashi, Y., Ueno, Y., Naraoka, H., Tomita, M., and Nishioka, T. (2003). Quantitative metabolome analysis using capillary electrophoresis mass spectrometry. J. Proteome Res. *2*, 488–494.

44. Soga, T., Ishikawa, T., Igarashi, S., Sugawara, K., Kakazu, Y., and Tomita, M. (2007). Analysis of nucleotides by pressure-assisted capillary electrophoresis-mass spectrometry using silanol mask technique. J. Chromatogr. A *1159*, 125–133.

45. Ingalls, A.M., Dickie, M.M., and Snell, G.D. (1950). Obese, a new mutation in the house mouse. J. Hered. *41*, 317–318.

46. Lindström, P. (2007). The physiology of obese-hyperglycemic mice [ob/ob mice]. ScientificWorldJournal *7*, 666–685.

47. Heinrich, R., and Rapoport, T.A. (1974). A linear steady-state treatment of enzymatic chains. General properties, control and effector strength. Eur. J. Biochem. *42*, 89–95.

48. Liebermeister, W., Uhlendorf, J., and Klipp, E. (2010). Modular rate laws for enzymatic reactions: thermodynamics, elasticities and implementation. Bioinformatics *26*, 1528–1534.

49. Noor, E., Flamholz, A., Liebermeister, W., Bar-Even, A., and Milo, R. (2013). A note on the kinetics of enzyme action: A decomposition that highlights thermodynamic effects. FEBS Lett. *587*, 2772–2777.

1108 50. Hofmeyr, J.H., and Cornish-Bowden, A. (1996). Co-response analysis: a new
1109 experimental strategy for metabolic control analysis. J. Theor. Biol. *182*, 371–380.

1110 51. Chang, A., Jeske, L., Ulbrich, S., Hofmann, J., Koblitz, J., Schomburg, I., Neumann-
1111 Schaal, M., Jahn, D., and Schomburg, D. (2021). BRENDA, the ELIXIR core data
1112 resource in 2021: new developments and updates. Nucleic Acids Res. *49*, D498–D508.

1113 52. Schuetz, R., Zamboni, N., Zampieri, M., Heinemann, M., and Sauer, U. (2012).
1114 Multidimensional Optimality of Microbial Metabolism. Science *336*, 601–604.

1115 53. De Martino, D., Figliuzzi, M., De Martino, A., and Marinari, E. (2012). A scalable
1116 algorithm to explore the Gibbs energy landscape of genome-scale metabolic networks.
1117 PLoS Comput. Biol. *8*, e1002562.

1118 54. Mahamkali, V., McCubbin, T., Beber, M.E., Noor, E., Marcellin, E., and Nielsen, L.K.
1119 (2021). multiTFA: a Python package for multi-variate thermodynamics-based flux
1120 analysis. Bioinformatics *37*, 3064–3066.

1121 55. Beber, M.E., Gollub, M.G., Mozaffari, D., Shebek, K.M., Flamholz, A.I., Milo, R., and
1122 Noor, E. (2022). eQuilibrator 3.0: a database solution for thermodynamic constant
1123 estimation. Nucleic Acids Res. *50*, D603–D609.

1124 56. Tanner, L.B., Goglia, A.G., Wei, M.H., Sehgal, T., Parsons, L.R., Park, J.O., White, E.,
1125 Toettcher, J.E., and Rabinowitz, J.D. (2018). Four key steps control glycolytic flux in
1126 mammalian cells. Cell Syst. *7*, 49-62.e8.

1127 57. Groen, A.K., van Roermund, C.W., Vervoorn, R.C., and Tager, J.M. (1986). Control of
1128 gluconeogenesis in rat liver cells. Flux control coefficients of the enzymes in the
1129 gluconeogenic pathway in the absence and presence of glucagon. Biochem. J *237*, 379–
1130 389.

1131 58. Rigoulet, M., Leverve, X.M., Plomp, P.J., and Meijer, A.J. (1987). Stimulation by
1132 glucose of gluconeogenesis in hepatocytes isolated from starved rats. Biochem. J. *245*,
1133 661–668.

1134 59. Fan, W., Hao, Y., Hou, X., Ding, C., Huang, D., Zheng, W., and Dai, Z. (2025).
1135 Unraveling principles of thermodynamics for genome-scale metabolic networks using
1136 graph neural networks. Cell Syst. *16*, 101393.

1137 60. Park, J.O., Tanner, L.B., Wei, M.H., Khana, D.B., Jacobson, T.B., Zhang, Z., Rubin, S.A.,
1138 Li, S.H.-J., Higgins, M.B., Stevenson, D.M., et al. (2019). Near-equilibrium glycolysis
1139 supports metabolic homeostasis and energy yield. Nat. Chem. Biol. *15*, 1001–1008.

1140 61. Milani, M., Pesce, A., Bolognesi, M., Bocedi, A., and Ascenzi, P. (2003). Substrate
1141 channeling: Molecular bases. Biochem. Mol. Biol. Educ. *31*, 228–233.

62. Datta, A., Merz, J.M., and Spivey, H.O. (1985). Substrate channeling of oxalacetate in solid-state complexes of malate dehydrogenase and citrate synthase. J. Biol. Chem. *260*, 15008–15012.

63. Wu, F., and Minteer, S. (2015). Krebs cycle metabolon: structural evidence of substrate channeling revealed by cross-linking and mass spectrometry. Angew. Chem. Int. Ed Engl. *54*, 1851–1854.

64. Anderson, L.E., Goldhaber-Gordon, I.M., Li, D., Tang, X.Y., Xiang, M., and Prakash, N. (1995). Enzyme-enzyme interaction in the chloroplast: glyceraldehyde-3-phosphate dehydrogenase, triose phosphate isomerase and aldolase. Planta *196*, 245–255.

65. Araiza-Olivera, D., Chiquete-Felix, N., Rosas-Lemus, M., Sampedro, J.G., Peña, A., Mujica, A., and Uribe-Carvajal, S. (2013). A glycolytic metabolon in Saccharomyces cerevisiae is stabilized by F-actin. FEBS J. *280*, 3887–3905.

66. Li, D., Morita, K., Kokaji, T., Hatano, A., Hirayama, A., Soga, T., Suzuki, Y., Matsumoto, M., Tsuchiya, T., Ozaki, H., et al. (2025). Global loss of responsiveness in key regulator metabolites and elevated enzyme proteins as metabolic dysregulation in skeletal muscle and liver of obese mice during starvation. bioRxiv, 2025.01.22.634184. https://doi.org/10.1101/2025.01.22.634184.

67. Bordbar, A., Feist, A.M., Usaite-Black, R., Woodcock, J., Palsson, B.O., and Famili, I. (2011). A multi-tissue type genome-scale metabolic network for analysis of whole-body systems physiology. BMC Syst. Biol. *5*. https://doi.org/10.1186/1752-0509-5-180.

68. Lancha, A.H., Jr, Recco, M.B., and Curi, R. (1994). Pyruvate carboxylase activity in the heart and skeletal muscles of the rat. Evidence for a stimulating effect of exercise. Biochem. Mol. Biol. Int. *32*, 483–489.

69. Minet, A.D., and Gaster, M. (2010). Pyruvate carboxylase is expressed in human skeletal muscle. Biochem. Biophys. Res. Commun. *402*, 196–197.

70. Noor, E., Haraldsdóttir, H.S., Milo, R., and Fleming, R.M.T. (2013). Consistent Estimation of Gibbs Energy Using Component Contributions. PLoS Comput. Biol. *9*. https://doi.org/10.1371/journal.pcbi.1003098.

71. Schuster, S., and Heinrich, R. (1991). Minimization of intermediate concentrations as a suggested optimality principle for biochemical networks: I. Theoretical analysis. J. Math. Biol. *29*, 425–442.

72. Gurobi Optimization, L.L.C. (2024). Gurobi Optimizer Reference Manual. https://www.gurobi.com/.

73. Hastie, T., Tibshirani, R., and Friedman, J. (2009). The elements of statistical learning: Data mining, inference, and prediction, second edition 2nd ed. (Springer).

74. Haraldsdóttir, H.S., Thiele, I., and Fleming, R.M.T. (2012). Quantitative assignment of reaction directionality in a multicompartmental human metabolic reconstruction. Biophys. J. *102*, 1703–1711.

75. Burgess, S.C., Jeffrey, F.M.H., Storey, C., Milde, A., Hausler, N., Merritt, M.E., Mulder, H., Holm, C., Sherry, A.D., and Malloy, C.R. (2005). Effect of murine strain on metabolic pathways of glucose production after brief or prolonged fasting. Am. J. Physiol. Endocrinol. Metab. *289*, E53-61.

76. Satapati, S., Sunny, N.E., Kucejova, B., Fu, X., He, T.T., Méndez-Lucas, A., Shelton, J.M., Perales, J.C., Browning, J.D., and Burgess, S.C. (2012). Elevated TCA cycle function in the pathology of diet-induced hepatic insulin resistance and fatty liver. J. Lipid Res. *53*, 1080–1092.

77. Hasenour, C.M., Wall, M.L., Ridley, D.E., Hughey, C.C., James, F.D., Wasserman, D.H., and Young, J.D. (2015). Mass spectrometry-based microassay of (2)H and (13)C plasma glucose labeling to quantify liver metabolic fluxes in vivo. Am. J. Physiol. Endocrinol. Metab. *309*, E191-203.

78. Hasenour, C.M., Rahim, M., and Young, J.D. (2020). In vivo estimates of liver metabolic flux assessed by 13C-propionate and 13C-lactate are impacted by tracer recycling and equilibrium assumptions. Cell Rep. *32*, 107986.

79. Wang, Y., Kwon, H., Su, X., and Wondisford, F.E. (2020). Glycerol not lactate is the major net carbon source for gluconeogenesis in mice during both short and prolonged fasting. Molecular Metabolism *31*, 36–44.

80. Turner, S.M., Linfoot, P.A., Neese, R.A., and Hellerstein, M.K. (2005). Sources of plasma glucose and liver glycogen in fasted ob/ob mice. Acta Diabetol. *42*, 187–193.

81. Haldane, J.B.S. (1930). Enzymes (Longmans, Green and Co.).

82. Cousins, B. (2022). Volume-and-Sampling - File Exchange - MATLAB CentralFile Exchange - MATLAB Central. https://www.mathworks.com/matlabcentral/fileexchange/43596-volume-and-sampling.

83. Ohno, S., Quek, L.-E., Krycer, J.R., Yugi, K., Hirayama, A., Ikeda, S., Shoji, F., Suzuki, K., Soga, T., James, D.E., et al. (2020). Kinetic trans-omic analysis reveals key regulatory mechanisms for insulin-regulated glucose metabolism in adipocytes. iScience *23*, 101479.

84. Lubitz, T., Schulz, M., Klipp, E., and Liebermeister, W. (2010). Parameter balancing in kinetic models of cell metabolism. J. Phys. Chem. B *114*, 16298–16303.

85. UniProt Consortium (2023). UniProt: The universal protein knowledgebase in 2023. Nucleic Acids Res. *51*, D523–D531.

86. Evan (2025). Plot Groups of Stacked Bars - File Exchange - MATLAB CentralFile Exchange - MATLAB Central. https://jp.mathworks.com/matlabcentral/fileexchange/32884-plot-groups-of-stacked-bars.

SUPPLEMENTAL INFORMATION

Figures S1 to S6

Tables S1 to S7

References (*87*) to (*97*)

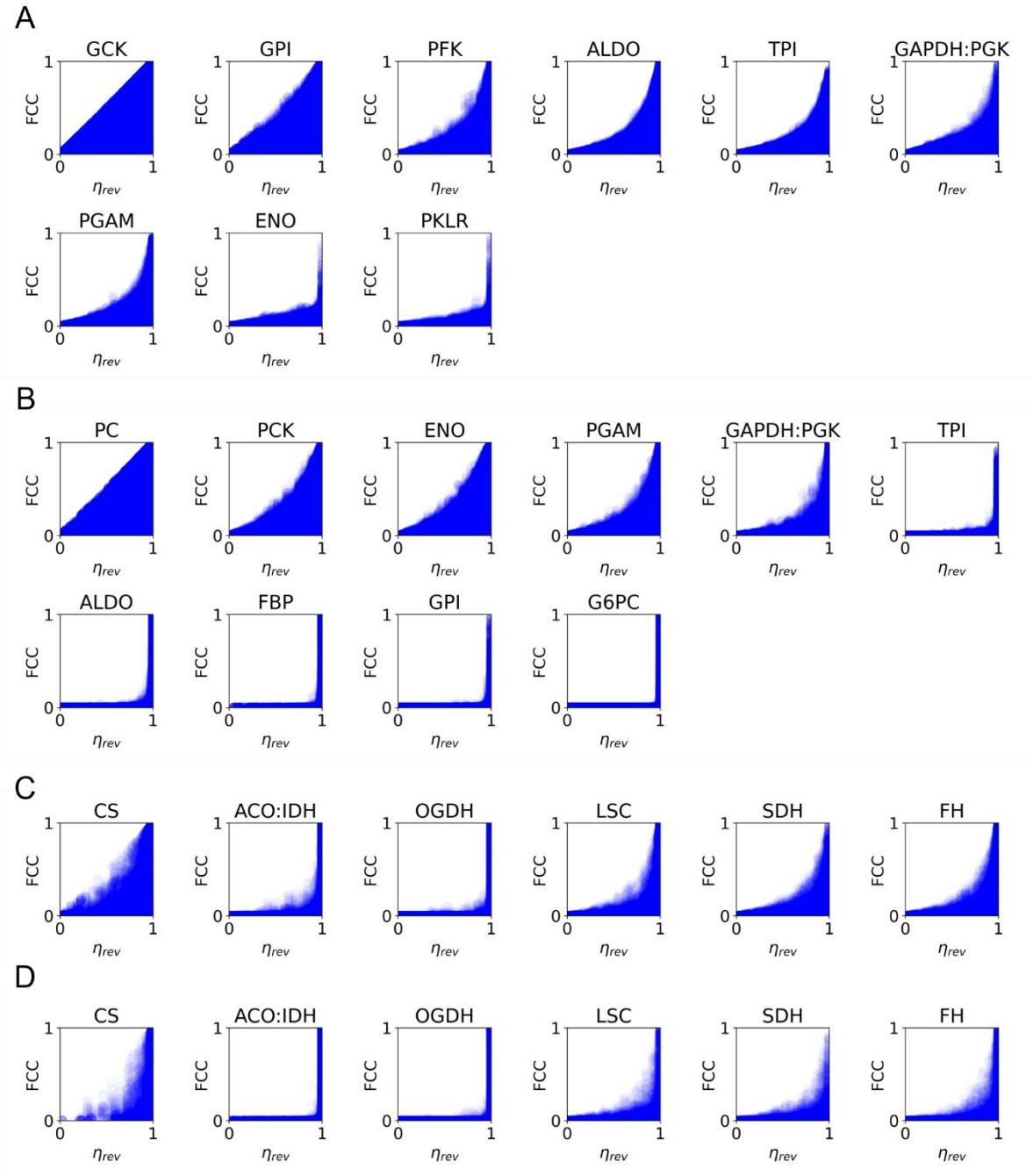

Fig. S1: Relationship between $\eta_{\mathbf{rev}}$ and FCC for arbitrary $\Delta_r G'$ landscapes

(**A-D**) Arbitrary $\Delta_r G'$ landscapes were generated by the uniform sampling of intrasellar metabolite concentrations under the blood metabolite concentrations at *ad libitum* feeding

1226 and after 16-hour fasting (see Methods). The arbitrary $\Delta_r G'$ landscapes at *ad libitum* feeding
1227 were used for FCC calculation in glycolysis (**A**) and the TCA cycle (**C**), while those after 16-
1228 hour fasting were used for gluconeogenesis (**B**), and the TCA cycle (**D**). Plotted data
1229 represents each sampled set of metabolite concentrations and $\Delta_f G'^{\circ}$, and K_{m} values.
1230

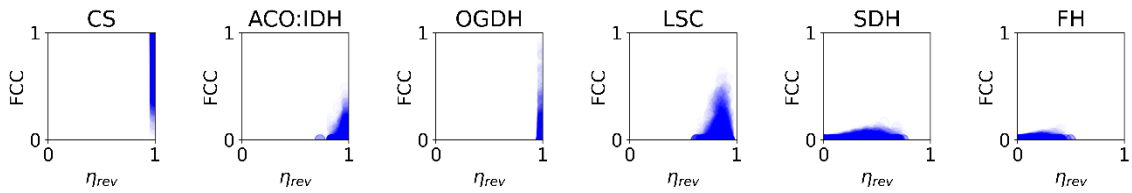

Fig. S2: Relationship between $\eta_{\mathbf{rev}}$ and FCC in the TCA cycle in the mouse liver after 16-hour fasting

Plotted data represents each set of metabolite concentrations and $\Delta_f G'^{\circ}$ values sampled for the calculation of confidence intervals, and K_{m} values sampled based on BRENDA database (see Methods).

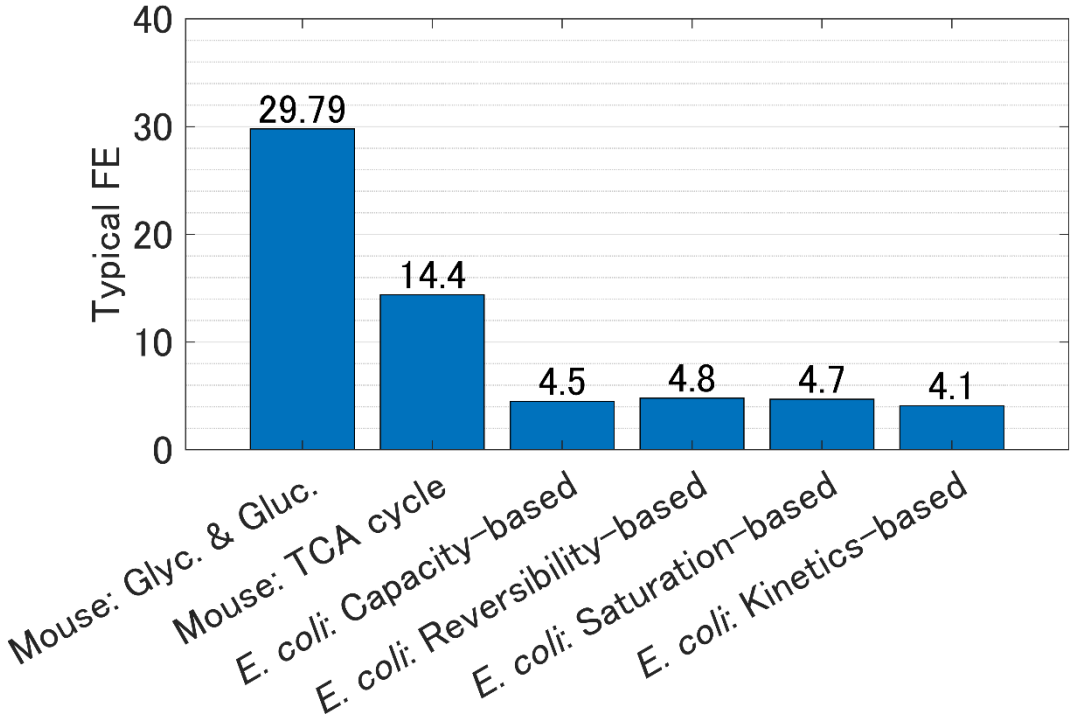

Fig. S3: Typical fold error of ECM's prediction compared to metabolite concentrations in the mouse liver and *E. coli*

Glyc. and Gluc. means glycolysis and gluconeogenesis, respectively. Minimizations of total EC in *E. coli* were conducted for the metabolic network, which consists of glycolysis, the pentose phosphate pathway, and the TCA cycle, assuming four different enzymatic rate laws (see Methods).

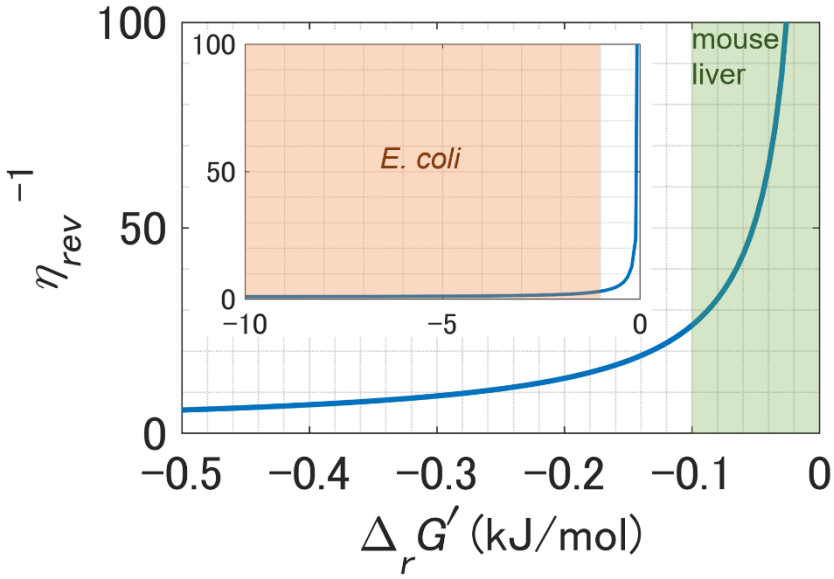

Fig. S4: Correspondence between $\Delta_r G'$ and η_{rev}^{-1}

Orange and green area depict the range of $\Delta_r G'$ that most reversible reactions in glycolysis exhibited in *E. coli* [26,60] and mouse liver, respectively.

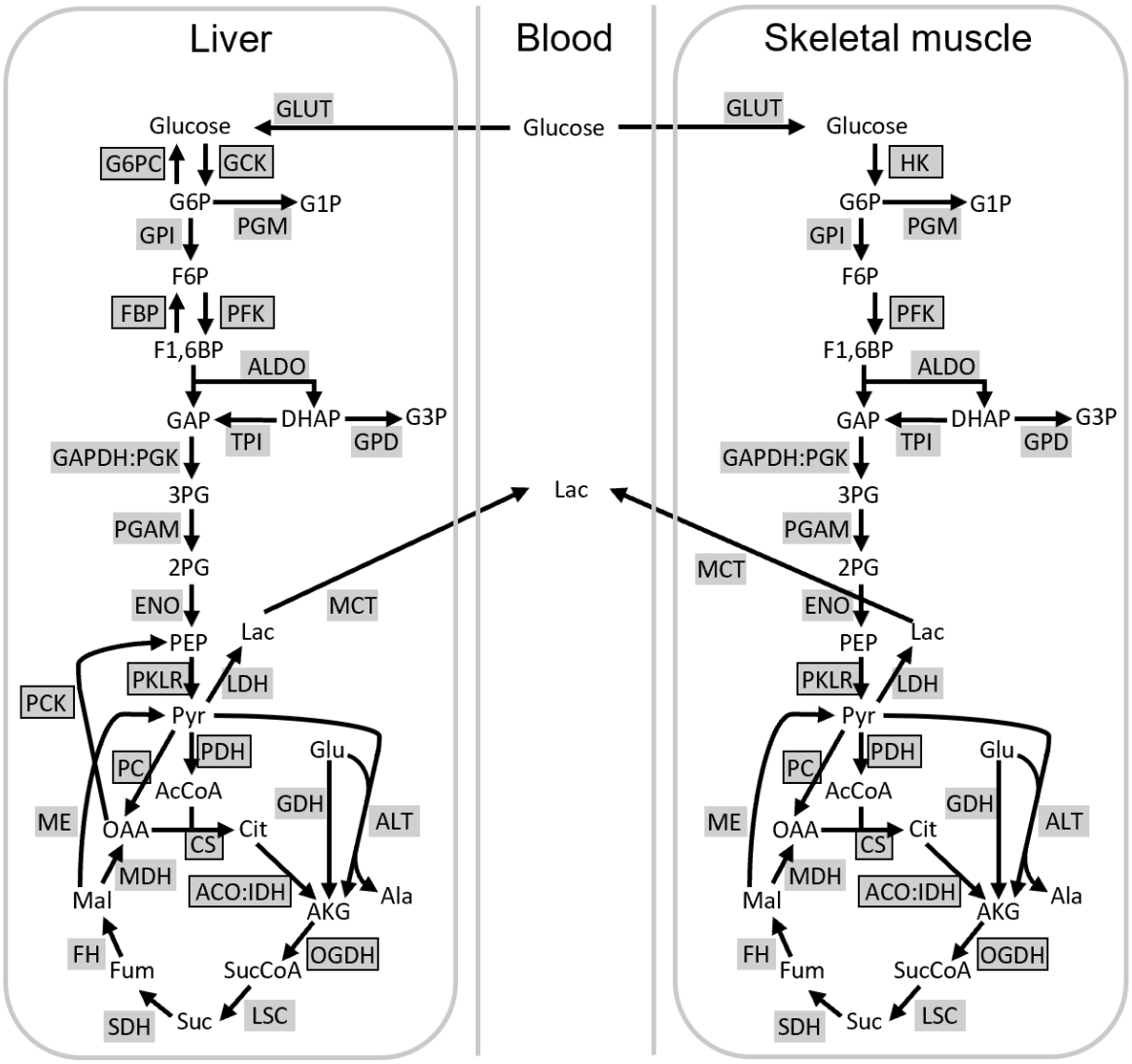

Fig. S5: A whole metabolic network used to estimate $\Delta_r G'$ landscape

Shaded texts represent reaction names; boxed reactions are irreversible, while unboxed reactions are reversible. Unshaded texts represent metabolites. Although the network consists of liver, blood, and skeletal muscle to improve the accuracy of $\Delta_f G'^{\circ}$ estimation, only the $\Delta_r G'$ landscape of reactions and transporters in the liver were discussed in this study because the concentration of unmeasured major metabolites, such as glucose in skeletal muscle, cannot be estimated with sufficient accuracy due to a lack of reactions.

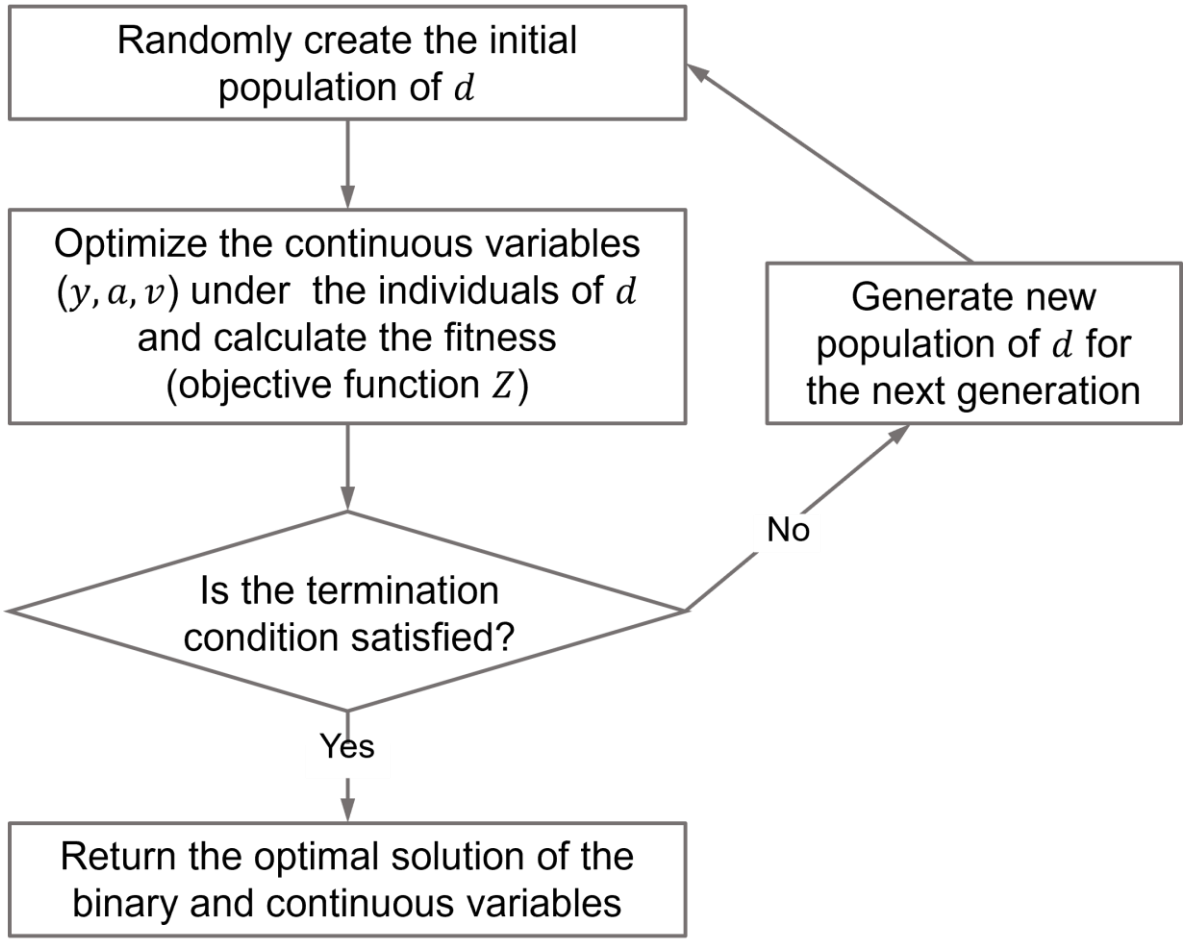

Fig. S6: Flowchart of the bilevel optimization problem in GLEAM

The optimization problems for the continuous and binary variables are treated as the lower-level and upper-level problems, respectively. The optimal solution of GLEAM was selected after solving this bilevel optimization 10 times.

1265 **SUPPLEMENTAL TABLES**

1266 **Table S1: Metabolomic and $\Delta_f G'^\circ$ data used as input for GLEAM (Excel file)**

1267 This file includes the input metabolomic and $\Delta_f G'^\circ$ data for GLEAM (logarithmic mean of
1268 metabolome concentrations, $\Delta_f G'^\circ$ values, and variance-covariance matrix of metabolite
1269 concentrations and $\Delta_f G'^\circ$s). The metabolite concentrations were measured form from WT
1270 and *ob*/*ob* mice in previous studies [8,66], and $\Delta_f G'^\circ$ data were retrieved from eQuilibrator
1271 database [55]. NaN represents unmeasured metabolite. [h], [m], and [b] indicate hepatic,
1272 myocytic, and blood compartment, respectively. The logarithmic mean of metabolite
1273 concentrations shown in this file is converted from a logarithmic scale to a linear scale.

1274

1275 **Table S2: Thermodynamically consistent metabolite concentrations, $\Delta_f G'^\circ$, and $\Delta_r G'$**
1276 **estimated by GLEAM (Excel file)**

1277 This file includes the thermodynamically consistent metabolite concentrations, $\Delta_f G'^\circ$, and
1278 $\Delta_r G'$ values in mouse liver and blood estimated by GLEAM. For glucose and lactate, hepatic
1279 and blood metabolites are distinguished by the [h] and [b], respectively.

1280

1281 **Table S3: Metabolites and reactions in the metabolic network for glucose metabolism**
1282 **in mice (Excel file)**

1283 This file includes definitions of metabolite abbreviations, reaction abbreviations, and the
1284 metabolic network *i.e.*, the stoichiometric matrix for glucose metabolism used in this study.
1285 In the Reactions and Stoichiometric matrix sheet, [h], [m], and [b] indicate hepatic, myocytic,
1286 and blood compartments, respectively.

1287

1288 **Table S4: Metabolite concentrations and a cofactor ratio involved in PKLR between**
1289 **mouse liver and other cell types**

Metabolites, cofacer ratios	Mouse liver	iBMK cell	Yeast	*E. coli*
PEP	2.02×10^{-5} M	1.16×10^{-5} M	2.91×10^{-5} M	1.84×10^{-4} M
Pyr	3.77×10^{-5} M	5.88×10^{-3} M	9.40×10^{-3} M	3.66×10^{-3} M
ATP/ADP	1.00	8.21	3.95	17.35

1290 Metabolite concentrations in iBMK cell, Yeast, and E. coli were measured by LC-MS [26].

1291

1292 **Table S5: EC calculation in mouse liver and ECM (Excel file)**

1293 This file includes EC values within glycolysis, gluconeogenesis, and the TCA cycle in mouse
1294 liver and EC, metabolite concentrations in ECM, and geometric mean of Michaelis-Menten
1295 constant retrieved from BRENDA database [51] used for EC calculation. In EC calculation,
1296 metabolite concentrations at *ad libitum* feeding were used for glycolysis and the TCA cycle,
1297 and those after 16-hour fasting were used for gluconeogenesis and the TCA cycle. EC is
1298 product of normalized molecular weight, $1/\eta_{\mathrm{rev}}$, and $1/\eta_{\mathrm{sat,s}}$.

1299

1300 **Table S6: Metabolite concentrations where the reactions required to reverse for**
1301 **metabolic switching are at equilibrium, as determined by MEG calculation (Excel file)**

1302 This file includes the metabolite concentrations that are the optimal solution to the
1303 optimization problem in MEG calculation for glycolysis, gluconeogenesis, and the TCA
1304 cycle. At these concentrations, the reactions required to reverse for directional switching of
1305 the pathways are at equilibrium with the minimum concentration changes from mouse liver
1306 or ECM.

1307

1308 **Table S7: Upper and lower bounds of metabolite concentrations and cofactor ratios**

Metabolites, cofacer ratios	Lower bounds	Upper bounds	References
Intracellular glucose*	1.0×10^{-3} M	1.5×10^{-2} M	87
Hepatic Pi	3.0×10^{-3} M	4.3×10^{-3} M	88
Myocytic Pi	3.0×10^{-3} M	9.0×10^{-3} M	88,89
CO_2, HCO_3^-	1.5×10^{-3} M	2.5×10^{-3} M	90
NH_3	2.0×10^{-4} M	1.0×10^{-3} M	91
Other intracellular metabolites*	1.0×10^{-7} M	1.0×10^{-2} M	26
Blood metabolites	1.0×10^{-7} M	1.0×10^{-1} M	92
ATP/ADP	1	10	89,93,94
NAD^+/NADH	3	10	95
GTP/GDP	1	10	96
$NADP^+$/NADPH	0.05	0.2	97

1309 *: The upper bounds of intracellular glucose, G6P, F6P, F1,6BP, DHAP, GAP, 3PG, 2PG,

1310 PEP, G1P, G3P, and Lac in *ob*/*ob* mouse are 1.0×10^{-1} M.

1311 **SUPPLEMENTAL REFERENCES**

1312 87. Wals, P.A., and Katz, J. (1993). A concentration gradient of glucose from liver to plasma.
1313 Metabolism *42*, 1492–1496.

1314 88. Till, U., Brox, D., and Frunder, H. (1969). Orthophosphate turnover in the extracellular
1315 and intracellular space of mouse liver. Eur. J. Biochem. *11*, 541–548.

1316 89. Veech, R.L., Lawson, J.W., Cornell, N.W., and Krebs, H.A. (1979). Cytosolic
1317 phosphorylation potential. J. Biol. Chem. *254*, 6538–6547.

1318 90. Beard, D.A., and Qian, H. (2005). Thermodynamic-based computational profiling of
1319 cellular regulatory control in hepatocyte metabolism. American Journal of Physiology-
1320 Endocrinology and Metabolism *288*, E633–E644.

1321 91. Meijer, A.J., Lamers, W.H., and Chamuleau, R.A. (1990). Nitrogen metabolism and
1322 ornithine cycle function. Physiol. Rev. *70*, 701–748.

1323 92. Ando, H., Ushijima, K., Shimba, S., and Fujimura, A. (2016). Daily Fasting Blood
1324 Glucose Rhythm in Male Mice: A Role of the Circadian Clock in the Liver.
1325 Endocrinology *157*, 463–469.

1326 93. Mörikofer-Zwez, S., and Walter, P. (1989). Binding of ADP to rat liver cytosolic proteins
1327 and its influence on the ratio of free ATP/free ADP. Biochem. J *259*, 117–124.

1328 94. Traut, T.W. (1994). Physiological concentrations of purines and pyrimidines. Mol. Cell.
1329 Biochem. *140*, 1–22.

1330 95. Lin, S.-J., and Guarente, L. (2003). Nicotinamide adenine dinucleotide, a metabolic
1331 regulator of transcription, longevity and disease. Curr. Opin. Cell Biol. *15*, 241–246.

1332 96. Bos, J.L., Rehmann, H., and Wittinghofer, A. (2007). GEFs and GAPs: Critical
1333 Elements in the Control of Small G Proteins. Cell *129*, 865–877.

1334 97. Veech, R.L., Eggleston, L.V., and Krebs, H.A. (1969). The redox state of free
1335 nicotinamide–adenine dinucleotide phosphate in the cytoplasm of rat liver. Biochem. J
1336 *115*, 609–619.